

## Linear Polarization of the 21 cm Line from the Epoch of Reionization

BOHUA LI <sup>1</sup>, JIANRONG TAN <sup>1,2</sup> AND YI MAO <sup>1</sup>

<sup>1</sup>*Department of Astronomy, Tsinghua University, Beijing, 100084, China*

<sup>2</sup>*Department of Physics & Astronomy, University of Pennsylvania, 209 South 33rd Street, Philadelphia, PA 19104, USA*

### ABSTRACT

The 21 cm linear polarization due to Thomson scattering off free electrons can probe the distribution of neutral hydrogen in the intergalactic medium during the epoch of reionization, complementary to the 21 cm temperature fluctuations. Previous study (Babich & Loeb 2005) estimated the strength of polarization with a toy model and claimed that it can be detected with 1-month observation of the Square Kilometre Array (SKA). Here we revisit this investigation with account of nonlinear terms due to inhomogeneous reionization, using seminumerical reionization simulations to provide the realistic estimation of the 21 cm TE and EE angular power spectra ( $C_\ell^{\text{TE}}$  and  $C_\ell^{\text{EE}}$ ). We find that (1) both power spectra are enhanced on sub-bubble scales but suppressed on super-bubble scales, compared with previous results; (2)  $C_\ell^{\text{TE}}$  displays a zero-crossing at  $\ell < 100$ , and its angular scale is sensitive to the scale-dependence of H I bias on large scales; (3) the ratios of the power spectrum to its maximum value during reionization at a given  $\ell$ , i.e.  $C_\ell^{\text{TE}}/C_{\ell,\text{max}}^{\text{TE}}$  and  $C_\ell^{\text{EE}}/C_{\ell,\text{max}}^{\text{EE}}$ , show robust correlations with the global ionized fraction. However, measurement of this signal will be very challenging not only because the overall strength is weaker than the sensitivity of SKA, but also because of the polarized foregrounds from diffuse synchrotron emission, and Faraday rotation which modifies the observed polarization. Nevertheless, the 21 cm linear polarization signal may still likely be detectable through other approaches, e.g. its cross-correlation with other probes.

*Keywords:* Reionization (1383), H I line emission (690), Radio interferometry (1346), Intergalactic medium (813), Large-scale structure of the universe (902), Two-point correlation function (1951)

### 1. INTRODUCTION

The epoch of reionization (EoR) is a major phase transition of the Universe, during which the neutral hydrogen in the intergalactic medium (IGM) is heated and ionized by ultraviolet and X-ray photons from the first luminous objects. The process of cosmic reionization involves the formation of the large-scale structure and the rich astrophysics associated with the formation of first luminous objects. Current constraints on the EoR (Bouwens et al. 2015; Robertson et al. 2015; Finkelstein et al. 2019) are from robust but indirect probes, e.g., the observations of high-redshift quasar spectra (e.g., Fan et al. 2006; McGreer et al. 2015; Becker et al. 2015), and the electron scattering optical depth to the cosmic microwave background (CMB) (Planck 2018 results VI.

Cosmological parameters), in the sense that these probes are only sensitive to some, but not all, information of the EoR.

The most promising direct avenue of probing the EoR is the intensity mapping of the redshifted 21 cm line due to the hyperfine transition of atomic hydrogen (e.g., Pritchard & Loeb 2012), because the 21 cm tomography can map the distribution of neutral hydrogen (H I) for a broad range of redshifts along the light cone. This tomographic mapping, which reveals the global history and morphological structure of cosmic reionization, contains a wealth of information regarding the structure formation of the Universe (e.g., Scott & Rees 1990; McQuinn et al. 2006; Mao et al. 2008; Chen et al. 2019), and the properties of the first galaxies and quasars as the source of reionization (e.g., Baek et al. 2010; Ahn et al. 2015; Dixon et al. 2016).

The next decades will be a golden age for the 21 cm observations. Current interferometric arrays, e.g. the Murchison Wide field Array (MWA, Tingay et al. 2013),

the LOw Frequency Array (LOFAR, [van Haarlem et al. 2013](#)), the Precision Array for Probing the Epoch of Reionization (PAPER, [Parsons et al. 2010](#)), and the Giant Metrewave Radio Telescope (GMRT, [Intema et al. 2017](#)), have first attempted to put upper limits on the 21 cm power spectrum from the EoR ([Paciga et al. 2013](#); [Pober et al. 2015](#); [Mertens et al. 2020](#); [Trott et al. 2020](#)). The next-generation radio interferometer arrays, including the Hydrogen Epoch of Reionization Array (HERA, [DeBoer et al. 2017](#)) and the Square Kilometre Array (SKA, [Mellema et al. 2013](#); [Koopmans et al. 2015](#)), promise to measure the statistical fluctuations of the 21 cm signal from the EoR for the first time. Furthermore, the SKA will very likely have enough sensitivity to generate the tomographic 21 cm maps.

The major efforts in the 21 cm modeling and data analysis (e.g., [Madau et al. 1997](#); [Furlanetto et al. 2004a](#); [Morales & Hewitt 2004](#); [Lidz et al. 2008](#); [Hoffmann et al. 2019](#); [Liu & Shaw 2020](#)) have hitherto focused on the total intensity (i.e. Stokes parameter  $I$ ) of the 21 cm brightness temperature. However, the polarization of the 21 cm radiation field (i.e. Stokes parameter  $Q$ ,  $U$  and  $V$ ), as a complementary probe to the 21 cm temperature field, also contains independent information of the EoR. In fact, radio interferometers, as constructed by pairs of orthogonal dipole antennae, can be sensitive to the polarization information after careful calibration ([Liu & Shaw 2020](#)). Thorough investigations of the 21 cm polarization signal, therefore, are worthwhile in order to obtain additional science returns from the interferometric observations. This paper is dedicated to the 21 cm *linear* polarization (i.e. Stokes parameter  $Q$  and  $U$ ) from the EoR. Note that the circular polarization (i.e. Stokes parameter  $V$ ) of the 21 cm signal can also be produced through some mechanisms, e.g. the Zeeman splitting of the triplet state by local magnetic fields ([Cooray & Furlanetto 2005](#)), and the splitting induced by the CMB quadrupole during the dark ages ([Hirata et al. 2018](#); [Ji et al. 2021](#)). However, the 21 cm circular polarization signal is subdominant during the EoR, and therefore not the focus of this paper.

[Babich & Loeb \(2005, hereafter BL05\)](#) pioneered the study of the 21 cm linear polarization signal, and discussed two categories of production mechanisms — intrinsic and secondary mechanisms. In principle, anisotropic Ly $\alpha$  pumping can produce a small signal of linear polarization intrinsically, i.e. at the time of emission of the 21 cm signal. The dominant effect, however, is due to the Thomson scattering of 21 cm photons off free electrons during the EoR. In analogy with the CMB polarization, the 21 cm radiation, even if unpolarized at the time of emission, will become partially linearly po-

larized when the scattering electrons see a quadrupole anisotropy in the temperature fluctuations, so this effect was called a secondary mechanism. In particular, for scalar perturbations, Thomson scattering only induces  $E$ -mode polarization due to symmetry argument.

BL05 studied the anisotropy of the 21 cm  $E$ -mode polarization and derived the EE and TE angular power spectra. As the first study of this subject, BL05 calculated the first-order components in the power spectrum, and employed a simple ansatz for the ionization power spectrum. On the observational side, BL05 forecast that the 21 cm TE power spectrum could be detected by the SKA with 1-month integration time, which might be too optimistic.

In this paper, we will revisit the formalism for the 21 cm linear polarization from the EoR, taking into account the nonlinear effects due to inhomogeneous reionization. These include (1) the coupling between the density fluctuations and the nonlinear ionization fraction fluctuations, and (2) the cross-power between the nonlinear H I field and the peculiar velocity field due to the redshift-space distortion (RSD) correction. We estimate the polarization signal with realistic modeling of the ionization power spectrum using the seminumerical simulation results. The formalism is kept in terms of the angular power spectrum,  $C_\ell$ , instead of the power spectrum,  $P(\vec{k})$ , since the former approach is more adapted to multifrequency studies and wide-field surveys ([Zaldarriaga et al. 2004](#); [Datta et al. 2007](#); [Liu et al. 2016](#)). We will investigate new features in the polarization angular power spectra, which may be used for constraining reionization. On the other hand, we will also reevaluate the detection prospects of the polarization signal by the upcoming SKA telescope, including a brief discussion on the effects of foregrounds, systematics, and Faraday rotation.

The rest of this paper is organized as follows. In §2, we reformulate the angular power spectra of the 21 cm linear polarization signal due to Thomson scattering, based on a fully relativistic framework, while leaving the detailed derivations to Appendices A, B, and C. We then describe the EoR modeling and our seminumerical simulations in §3 which provide the initial source fields for the 21 cm signal. In §4, we present the numerical results and discuss their cosmological implications. We briefly discuss the observational prospects of the polarization signal in §5, and make concluding remarks in §6.

## 2. THE 21 CM LINEAR POLARIZATION

### 2.1. Temperature anisotropy

Before showing the 21 cm temperature anisotropy, we briefly clarify all the approximations made in this paper.

- (1) The 21 cm lines are optically thin,  $\tau_{\nu_{\text{obs}}} \ll 1$  (e.g., Lewis & Challinor 2007).
- (2) The IGM has been preheated so that  $T_s \gg T_{\text{CMB}}$ . It is valid soon after reionization begins, when  $T_s$  quickly reaches above  $10^4$  K because of sufficient heating of the IGM due to X-ray photons, and efficient coupling of  $T_s$  with the kinetic temperature of the gas via Ly $\alpha$  pumping (e.g., Chen & Miralda-Escudé 2004; Furlanetto 2006; Baek et al. 2009).
- (3) During the EoR, matter fluctuations are still Gaussian and linear on most relevant scales,  $|\delta| \ll 1$ , whereas H I density fluctuations are not, due to reionization patchiness. This is the so-called “quasi-linear” regime (Mao et al. 2012).

Altogether, it is reasonable to assume the *optically-thin, post-heating, quasi-linear* regime for most emitting H I gases during the EoR<sup>1</sup>. We refer interested readers to the detailed implications of these assumptions in Appendix A.1.

Under these approximations, we can model the 21 cm brightness temperature at the observed frequency  $\nu_{\text{obs}}$  along the direction of  $\hat{n}$  as seen by an observer at  $(\eta_{\text{obs}}, \vec{x})$ , where  $\eta$  is the conformal time, as

$$\delta T_{\text{b}} \approx T_0(z) \bar{x}_{\text{HI,m}}(z_{\text{em}}) \left(1 + \delta_{\text{HI}}\right) \left(1 - \frac{1}{\mathcal{H}} \frac{\partial v_{\parallel}}{\partial r}\right). \quad (1)$$

In this expression, the terms responsible for the global signal include the *mass-weighted* average neutral fraction,  $\bar{x}_{\text{HI,m}} \equiv \bar{n}_{\text{HI}}/\bar{n}_{\text{H}}$ , at the redshift of emission  $z_{\text{em}}$ , and the dimensional factor  $T_0(z)$ , which we refer readers to Appendix A.3 for its definition. The fluctuations of the signal are determined by  $\delta_{\text{HI}}$  (the neutral hydrogen density fluctuations), and the LoS velocity gradient term,  $(1/\mathcal{H})(\partial v_{\parallel}/\partial r)$ , which accounts for the RSD effect, where  $v_{\parallel} \equiv \vec{v} \cdot \hat{r} = -\vec{v} \cdot \hat{n}$  is the LoS projection of the H I peculiar velocity at emission, and  $\mathcal{H} \equiv aH$  is the conformal Hubble parameter. The RSD term is small in the quasi-linear regime,  $|(1/\mathcal{H})(\partial v_{\parallel}/\partial r)| \sim |\delta| \ll 1$ . Here  $\delta$  is the gauge-dependent matter overdensity.

<sup>1</sup> The 21 cm signal from a fixed redshift or  $\nu_{\text{obs}}$  is also subject to the light-cone (LC) effect (e.g., Barkana & Loeb 2006). To exactly account for the LC anisotropy, one must resort to full numerical schemes (e.g., Mao et al. 2012; Mondal et al. 2018; Chapman & Santos 2019). However, the LC effect is important only for the longitudinal modes along the LoS, but our focus is the transverse 2D modes perpendicular to the LoS. Therefore, in this paper we will neglect the LC effect for the EoR signal, evaluating it at the ensemble-averaged radial distance of 21 cm emission events from all directions. Justification of this treatment can be found in more detail in Appendix A.2.

Our primary interest is the *fluctuations and anisotropies* of the signal. We define the dimensionless brightness temperature as  $\psi(\eta_{\text{obs}}, \vec{x}, \nu_{\text{obs}}, \hat{n}) \equiv \delta T_{\text{b}}(\eta_{\text{obs}}, \vec{x}, \nu_{\text{obs}}, \hat{n})/T_0(z)$ . The fluctuations and anisotropies of  $\psi$  are defined as  $\Theta(\eta_{\text{obs}}, \vec{x}, \nu_{\text{obs}}, \hat{n}) \equiv \psi/\langle\psi\rangle - 1$ . In Fourier space, its conjugate is (see the derivation in Appendix A.3)

$$\Theta(\eta_{\text{obs}}, \vec{k}, \nu_{\text{obs}}, \mu) \approx \delta_{\text{HI}}(\vec{k}, z_{\text{em}}) e^{-i\mu ks} + \mu^2 \delta(\vec{k}, z_{\text{em}}) e^{-i\mu ks}, \quad (2)$$

where  $\mu \equiv \hat{k} \cdot \hat{n}$  and  $s$  is the comoving radial distance in the redshift space.

The free-streaming projection of plane waves is manifest in Eq. (2). Consequently, multipole moments of temperature anisotropies can be defined in the  $\hat{z} = \hat{k}$  frame (so that  $\mu = \cos\theta$ ):

$$\Theta_{\ell}(\eta_{\text{obs}}, \vec{k}, \nu_{\text{obs}}) \equiv \frac{1}{(-i)^{\ell}} \int_{-1}^1 \frac{d\mu}{2} \mathcal{P}_{\ell}(\mu) \Theta(\eta_{\text{obs}}, \vec{k}, \nu_{\text{obs}}, \mu) = \delta_{\text{HI}}(\vec{k}, z_{\text{em}}) j_{\ell}(ks) - \delta(\vec{k}, z_{\text{em}}) j_{\ell}''(ks), \quad (3)$$

where  $\mathcal{P}_{\ell}(\mu)$  is the Legendre polynomial,  $j_{\ell}(x)$  is the spherical Bessel function, and  $j_{\ell}''(x)$  is the second-order derivative of  $j_{\ell}(x)$  with respect to its argument.

## 2.2. Linear polarization from electron scattering

Thomson scattering couples the intensity to the  $E$ -mode polarization, thereby generating the latter out of the unpolarized light. For scalar perturbations, the  $B$ -mode polarization is decoupled from the  $E$ -mode and vanishes under the azimuthal symmetry around  $\hat{k}$ . Analogous to the CMB, the transport of the 21 cm polarization signal follows the Boltzmann equations and its observed anisotropies can be calculated by the standard LoS integration formalism (Zaldarriaga & Seljak 1997; BL05). It exploits the multipole expansion (Eq. 3) in the  $\hat{z} = \hat{k}$  frame and yields the present-day observed (scalar) EE angular power spectrum, which is defined as  $C_{\ell}^{\text{EE}}(\eta_0, \nu_{\text{obs},0}) \equiv \langle |a_{E,\ell m}(\eta_0, \vec{x}_0, \nu_{\text{obs},0})|^2 \rangle$ , where  $a_{E,\ell m}$  are coefficients of the spherical harmonics decomposition. For a present-day Earth observer,

$$C_{\ell}^{\text{EE}}(\eta_0, \nu_{\text{obs},0}) = 4\pi \left\langle \left| \int \frac{d^3\vec{k}}{(2\pi)^3} \Delta_{E\ell}(\eta_0, \vec{k}, \nu_{\text{obs},0}) \right|^2 \right\rangle. \quad (4)$$

In the expression above,  $\Delta_{E\ell}$  are multipole moments of  $E$ -mode polarization anisotropies in the  $\hat{z} = \hat{k}$  frame, and are derived in the standard LoS integration formalism. Here we write down its expression as follows:

$$\Delta_{E\ell}(\eta_0, \vec{k}, \nu_{\text{obs},0}) \approx \frac{3}{4} \sqrt{\frac{(\ell+2)!}{(\ell-2)!}} \times \int_{\bar{\eta}_{z_{\text{em}}}}^{\bar{\eta}_0} g(\eta') \Pi(\eta', \vec{k}, \nu') \frac{j_{\ell}[ck(\bar{\eta}_0 - \eta')]}{[ck(\bar{\eta}_0 - \eta')]^2} d\eta', \quad (5)$$

where  $\nu' = \nu_{\text{obs},0}(1+z') \leq \nu_{21}$  is the frequency of 21 cm photons seen by an intervening free electron, and the source function  $\Pi(\eta', \vec{k}, \nu') = \Theta_2(\eta', \vec{k}, \nu') + \Delta_{P_2}(\eta', \vec{k}, \nu') + \Delta_{P_0}(\eta', \vec{k}, \nu')$ , where  $\Theta_2$  is the quadrupole moment of temperature fluctuations, and  $\Delta_{P_\ell}$  are multipole moments of the total linear polarization. The (global) visibility function is defined as  $g(\eta) \equiv -(d\tau/d\eta)e^{-\tau}$ , where  $\tau$  is the Thomson scattering optical depth,  $\tau(\eta) \equiv \int_\eta^{\eta_0} \bar{n}_e(\eta')\sigma_T c d\eta'$ ,  $\sigma_T$  is the Thomson scattering cross section.  $g(\eta)$  depends on the global ionization history, illustrated in §3.1. In Eq. (5), the density of free electrons is approximated by the globally-averaged value,  $\bar{n}_e$ . However, in reality their distribution is patchy during the EoR and may cause secondary polarization (see, e.g., Hu 2000; Doré et al. 2007, for the case of the CMB). This effect is worth further examinations but for now we neglect it as in BL05.

Given the low value of the electron scattering optical depth ( $\tau_{\text{es}} \sim 0.05$ ), it is reasonable to assume that

most of the 21 cm photons do not scatter more than once by free electrons before they reach the observer. As a result, the relevant source function  $\Pi$  for 21 cm polarization (with the CMB part subtracted off) only has the contribution from the incident quadrupole,  $\Theta_2$ . (Note that this is not the case for the CMB in the tight coupling limit). Also, under the current sensitivity of 21 cm experiments, the nuisance that the 21 cm temperature signal is suppressed by a factor of  $\exp(-\tau_{\text{es}})$  due to Thomson scattering can be neglected so that  $\Theta(\vec{k}, \mu)$  remains at the free-streaming value (Eq. 2).

On the other hand,  $\Theta$  from Eq. (2) can be viewed as a decomposition according to the initial source fields,  $\delta_{\text{HI}}$  and  $\delta$ , which are statistically homogeneous and isotropic. Each term has its own temperature transfer function:  $T_{\text{HI}}^{\text{T}}(\eta_{\text{obs}}, k, \nu_{\text{obs}}, \mu) = e^{-i\mu ks}$  and  $T_{\delta}^{\text{T}}(\eta_{\text{obs}}, k, \nu_{\text{obs}}, \mu) = \mu^2 e^{-i\mu ks}$ . Evidently, Eq. (3) implies that multipole moments of these temperature transfer functions are  $T_{\text{HI},\ell}^{\text{T}}(\eta_{\text{obs}}, k, \nu_{\text{obs}}) = j_\ell[ck(\bar{\eta}_{z_{\text{obs}}} - \bar{\eta}_{z_{\text{em}}})]$  and  $T_{\delta,\ell}^{\text{T}}(\eta_{\text{obs}}, k, \nu_{\text{obs}}) = -j'_\ell[ck(\bar{\eta}_{z_{\text{obs}}} - \bar{\eta}_{z_{\text{em}}})]$ .

Thus, the present-day EE power spectrum can be explicitly written as

$$C_\ell^{\text{EE}}(\eta_0, \nu_{\text{obs},0}) = \frac{2}{\pi} \int k^2 dk \left[ P_{\text{HI}}(k, z_{\text{em}}) (\mathcal{T}_{\text{HI},\ell}^{\text{E}}(k))^2 + P_\delta(k, z_{\text{em}}) (\mathcal{T}_{\delta,\ell}^{\text{E}}(k))^2 + 2P_{\text{HI}\delta}(k, z_{\text{em}}) \mathcal{T}_{\text{HI},\ell}^{\text{E}}(k) \mathcal{T}_{\delta,\ell}^{\text{E}}(k) \right]. \quad (6)$$

Here the multipole moments of the  $E$ -mode polarization transfer functions in the integrand of the RHS of Eq. (6), as well as those temperature transfer functions in the integrand of the RHS of Eq. (8–9) below, are all implicitly evaluated at  $(\eta_0, \nu_{\text{obs},0})$ ,

$$\mathcal{T}_{\text{HI},\ell}^{\text{E}}(\eta_0, k, \nu_{\text{obs},0}) \equiv \frac{3}{4} \sqrt{\frac{(\ell+2)!}{(\ell-2)!}} \int_{\bar{\eta}_{z_{\text{em}}}}^{\bar{\eta}_0} g(\eta') j_2[ck(\eta' - \bar{\eta}_{z_{\text{em}}})] \frac{j_\ell[ck(\bar{\eta}_0 - \eta')]}{[ck(\bar{\eta}_0 - \eta')]^2} d\eta', \quad (7a)$$

$$\mathcal{T}_{\delta,\ell}^{\text{E}}(\eta_0, k, \nu_{\text{obs},0}) \equiv -\frac{3}{4} \sqrt{\frac{(\ell+2)!}{(\ell-2)!}} \int_{\bar{\eta}_{z_{\text{em}}}}^{\bar{\eta}_0} g(\eta') j_2''[ck(\eta' - \bar{\eta}_{z_{\text{em}}})] \frac{j_\ell[ck(\bar{\eta}_0 - \eta')]}{[ck(\bar{\eta}_0 - \eta')]^2} d\eta'. \quad (7b)$$

Here  $P_{\text{HI}}$  and  $P_\delta$  are the (equal-time) H I density and matter power spectra, respectively, and  $P_{\text{HI}\delta}$  is the cross-power spectrum between the H I and the matter field. They are defined as  $\langle \delta_{\text{HI}}^*(\vec{k}) \delta_{\text{HI}}(\vec{k}') \rangle \equiv (2\pi)^3 P_{\text{HI}}(k) \delta_{\text{D}}^{(3)}(\vec{k} - \vec{k}')$ ,  $\langle \delta^*(\vec{k}) \delta(\vec{k}') \rangle \equiv (2\pi)^3 P_\delta(k) \delta_{\text{D}}^{(3)}(\vec{k} - \vec{k}')$ , and  $\langle \delta_{\text{HI}}^*(\vec{k}) \delta(\vec{k}') \rangle \equiv (2\pi)^3 P_{\text{HI}\delta}(k) \delta_{\text{D}}^{(3)}(\vec{k} - \vec{k}')$ . Finally, to obtain dimensional quantities, the extra coefficient of  $[T_0(z_{\text{em}}) \bar{x}_{\text{HI},m}(z_{\text{em}})]^2$  should be multiplied to the result of the dimensionless angular power spectrum.

Similarly, the temperature power spectrum observed today,  $C_\ell^{\text{TT}} = 4\pi \left\langle \left| \int d^3\vec{k} \Theta_\ell(\eta_0, k, \nu_{\text{obs},0}) / (2\pi)^3 \right|^2 \right\rangle$ , is given by

$$C_\ell^{\text{TT}}(\eta_0, \nu_{\text{obs},0}) = \frac{2}{\pi} \int k^2 dk \left[ P_{\text{HI}}(k, z_{\text{em}}) (T_{\text{HI},\ell}^{\text{T}}(k))^2 + P_\delta(k, z_{\text{em}}) (T_{\delta,\ell}^{\text{T}}(k))^2 + 2P_{\text{HI}\delta}(k, z_{\text{em}}) T_{\text{HI},\ell}^{\text{T}}(k) T_{\delta,\ell}^{\text{T}}(k) \right]. \quad (8)$$

The cross-power spectrum between the temperature and the  $E$ -mode polarization is

$$C_\ell^{\text{TE}}(\eta_0, \nu_{\text{obs},0}) = \frac{2}{\pi} \int k^2 dk \left\{ P_{\text{HI}}(k, z_{\text{em}}) T_{\text{HI},\ell}^{\text{T}}(k) \mathcal{T}_{\text{HI},\ell}^{\text{E}}(k) + P_\delta(k, z_{\text{em}}) T_{\delta,\ell}^{\text{T}}(k) \mathcal{T}_{\delta,\ell}^{\text{E}}(k) \right. \\ \left. + P_{\text{HI}\delta}(k, z_{\text{em}}) [T_{\text{HI},\ell}^{\text{T}}(k) \mathcal{T}_{\delta,\ell}^{\text{E}}(k) + T_{\delta,\ell}^{\text{T}}(k) \mathcal{T}_{\text{HI},\ell}^{\text{E}}(k)] \right\}. \quad (9)$$

Eqs. (6) and (9) describe the polarization signals that we seek in this paper. The case in which 21 cm bright-

ness temperature fluctuations are sourced by multiple

cosmological fields in a more general context is formulated in Appendix B.

### 2.3. Previous modeling of the 21 cm polarization

An equivalent way to write down the dimensionless brightness temperature is

$$\psi \equiv x_{\text{HI}} [1 + \Delta] = x_{\text{HI}} + \bar{x}_{\text{HI}} [\Delta + \delta x_{\text{HI}} \Delta], \quad (10)$$

where  $\Delta \equiv \delta - (1/\mathcal{H})(\partial v_{\parallel}/\partial r)$  and  $x_{\text{HI}}$  is the local neutral fraction. It is implicitly assumed that the baryon distribution follows that of the total matter. BL05 ignored the nonlinear coupling term  $\delta x_{\text{HI}} \Delta$ , so that they approximated  $\psi \approx x_{\text{HI}} + \bar{x}_{\text{HI}} \Delta$  and calculated the temperature multipole  $\bar{x}_{\text{HI},m}(z_{\text{em}}) \Theta_{\ell}(\eta_{\text{obs}}, \vec{k}, \nu_{\text{obs}})$  as

$$\bar{x}_{\text{HI}}(z_{\text{cm}}) \left[ \delta x_{\text{HI}}(\bar{\eta}_{z_{\text{em}}}, \vec{k}) j_{\ell}(ks) + \delta(\bar{\eta}_{z_{\text{em}}}, \vec{k}) \left( j_{\ell}(ks) - j_{\ell}''(ks) \right) \right]. \quad (11)$$

Also, the cross-power between the two terms on the RHS of Eq. (11) was missing from their modeling.

Nevertheless, both nonlinear term  $\delta x_{\text{HI}} \Delta$  and the cross-power  $P_{x_{\text{HI}} \delta}$  are non-negligible, since fluctuations in the ionization field is significant ( $\delta x_{\text{HI}} \sim 1$ ), as will be shown in §3.3 (see Figure 2). Our approach improves upon previous modeling by including not only the autocorrelations of the source fields (the ionization field and the corrections for the RSD), but also the contributions from cross-correlations  $P_{\text{HI} \delta}(k)$ . We leave a detailed comparison of formulations to Appendix C.

## 3. REIONIZATION MODELING

In the previous section, we focused on the accurate modeling of the 21 cm linear polarization signal from the EoR. In this section, we focus on modeling the inhomogeneous reionization that sources the 21 cm signal.

Generally, cosmic reionization began when the first structures formed around  $z \approx 30$  (e.g., Barkana & Loeb 2001; Dayal & Ferrara 2018). Each luminous source first creates an ionized region (“H II bubbles”) around itself. Ionized regions grow and later overlap, percolating into the IGM. The completion of bubble overlapping marks the end of reionization by  $z \sim 5 - 6$  (e.g., Mesinger 2010). For 21 cm polarization, the dominant source for the EoR signal is the ionization field, or equivalently, the neutral fraction field,  $\delta x_{\text{HI}} \equiv x_{\text{HI}}/\bar{x}_{\text{HI}} - 1$  ( $\bar{x}_{\text{HI}}$  is the *volume-weighted* average neutral fraction). It is patchy and nonlinear during the bulk of cosmic reionization, as supported by observations (Becker et al. 2015; Greig et al. 2017).

There are a variety of approaches to model the inhomogeneous ionization field, including analytical, seminumerical and fully-numerical methods. Early analytical

models often approximate two-point statistics of the ionization field with simplified, yet physically motivated ansatz (e.g., Gruzinov & Hu 1998; Knox et al. 1998). For example, BL05 employed a simple bubble model to estimate the neutral fraction power spectrum, which assumes that H II regions are randomly-distributed, fully-ionized spheres. Furlanetto et al. (2004b) introduced more sophisticated analytical model that is based on the excursion set formalism. This formalism relates the emissivity of ionizing sources to the underlying matter distribution. Based upon this scheme, efficient *seminumerical* algorithms have been developed to generate the realizations of ionization fields without the radiative transfer computations (e.g., Mesinger & Furlanetto 2007; Santos et al. 2010; Mesinger et al. 2011). Finally, to provide the most accurate modeling of reionization, one needs cosmological radiative transfer simulations and/or radiation-hydrodynamic simulations with large enough dynamical ranges and reasonable prescriptions for ionization sources (e.g., Iliev et al. 2006; McQuinn et al. 2007; Trac & Cen 2007; Baek et al. 2010; Battaglia et al. 2013; Rosdahl et al. 2013; Iliev et al. 2014; O’Shea et al. 2015; Ocvirk et al. 2016; Mao et al. 2020).

In this paper, we employ the seminumerical approach to estimate the ionization power spectra. It can model the effect of patchy reionization more realistically than analytical methods, and is computationally more efficient than fully-numerical methods. Moreover, comparisons between radiative transfer simulations and seminumerical simulations of reionization (e.g., Zahn et al. 2007, 2011; Majumdar et al. 2014; Hutter 2018) demonstrated that their predictions on the power spectrum agree with each other in reasonable accuracies at the scales of interest to upcoming interferometric observations. Thus, their difference should not affect the conclusions presented in this paper.

We present our seminumerical simulations in §3.1, briefly review early analytical models in §3.2, and discuss the H I power spectrum and H I bias in §3.3.

### 3.1. Seminumerical reionization simulations

The density fields and ionization fields are generated from cosmological seminumerical simulations of reionization using the 21cmFAST code<sup>2</sup> (Mesinger et al. 2011), with two choices of comoving boxes: the large box with 2000 cMpc per side and the small box with 512 cMpc per side. For the large (small) box, initial conditions are created on a  $4000^3$  ( $4096^3$ ) grid, and smoothed down to a  $1000^3$  ( $1024^3$ ) grid for the reionization simulation. We

<sup>2</sup> <https://github.com/andreimesinger/21cmFAST>

**Table 1.** EoR model parameters

Model	$\zeta$	$T_{\text{vir}}$ [K]	$R_{\text{mfp}}$ [cMpc]
1	30	$6 \times 10^4$	40
2	35	$1 \times 10^5$	40
3	40	$7 \times 10^4$	35

output data at desired redshifts during the post-heating phase of the EoR, ranging from  $z = 10$  to  $z = 5.6$ .

The simulations are based on three fundamental parameters in the EoR modeling:  $\zeta$  (ionization efficiency),  $T_{\text{vir}}$  (the minimum virial temperature of halos that host ionizing sources), and  $R_{\text{mfp}}$  (the maximum mean free path of ionizing photons). Detailed astrophysical interpretations of these parameters and how the global ionization history depends on them can be found in Mesinger et al. (2011); Greig & Mesinger (2017, 2018); Murray et al. (2020).

For both the large and small boxes, we apply multiple sets of EoR parameters, labeled as “Model 1-3” in Table 1.<sup>3</sup> They generate different global ionization histories, and thus different electron scattering optical depths and visibility functions (defined in §2.2). For each model in Table 1, we have verified that the global ionization histories from the two box sizes are consistent.

Figure 1 shows the ionization histories, compared with current model-independent observational constraints from (1) the fraction of “dark” pixels in the Ly $\alpha$  and Ly $\beta$  forests, and (2) the global Thomson optical depth inferred by the CMB.  $\bar{Q}_{\text{HII}} \equiv 1 - \bar{x}_{\text{HII}}$  defines the H II volume filling fraction (a.k.a. the global ionized fraction). The top and middle panels verify the physical dependence of the ionization history on the EoR parameters. For example, Model 2 has the highest  $T_{\text{vir}}$  among the three, resulting in the latest beginning of reionization and the lowest value of  $\tau_{\text{es}}$ . For Model 3, it has a higher ionization efficiency  $\zeta$  (and a slightly higher  $T_{\text{vir}}$ ) than Model 1, which leads to the earliest onset and end of reionization among the three. The bottom panel of Figure 1 shows that the visibility function, while reaching its maximum near the end of the EoR, demonstrates a broad width over redshift, in contrast to the sharply-peaked  $g(\eta)$  at recombination with respect to the CMB (Hu & Sugiyama 1995). Therefore, the LoS integra-

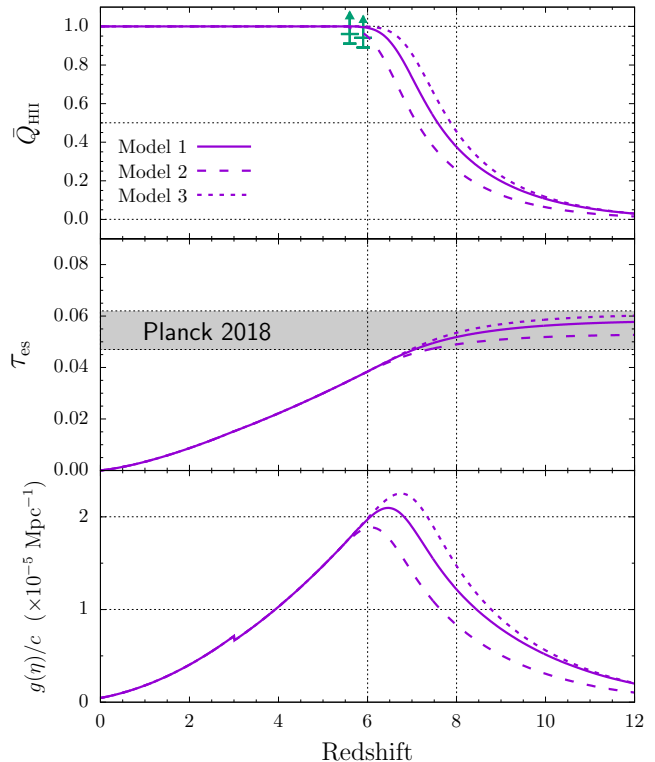


**Figure 1.** Reionization histories generated by the seminumerical simulations of reionization with EoR model parameters ( $\zeta, T_{\text{vir}}, R_{\text{mfp}}$ ) in Table 1 (solid/dashed/dotted curves for Model 1/2/3). Shown are the H II volume filling fraction  $\bar{Q}_{\text{HII}}$  (top), the CMB Thomson scattering optical depth  $\tau_{\text{es}}$  (middle), and the visibility function normalized by  $c$ ,  $g(\eta)/c$  (bottom), as a function of redshift. These reionization histories are all consistent with  $1\sigma$  constraints from the fraction of “dark” pixels in the Ly $\alpha$  and Ly $\beta$  forests (McGreer et al. 2015, arrows in the top panel) and the global  $\tau_{\text{es}}$  inferred by the CMB (Planck 2018 results VI. Cosmological parameters, the shaded area in the middle panel). In the bottom panel, the discontinuity at  $z = 3$  is due to He II reionization.

tion in Eqs. (7a–7b) is more time-consuming than in the CMB case.

### 3.2. Analytical models

For the purpose of comparison, here we review some of the early analytical models for the ionization field. BL05 made an assumption that at the end of the EoR (at  $z_{\text{re}}$ ), H II regions are approximately Poisson-randomly-distributed bubbles (BL05; De & Tashiro 2014). As a result, fluctuations in the ionized fraction are dominated by those in the local number of bubbles. Also, reionization is assumed to be instantaneous at  $z_{\text{re}}$ . Based on these assumptions, the ionization power spectrum  $P_x(k)$  (i.e. power spectrum of the neutral fraction field  $x_{\text{HII}}$ ) is estimated with the following ansatz at the end of the

<sup>3</sup> In this paper, we assume a  $\Lambda$ CDM cosmology with  $\Omega_{\text{m}} = 0.32$ ,  $\Omega_{\text{b}} = 0.05$ ,  $h = 0.67$ ,  $n_{\text{s}} = 0.97$  and  $\sigma_8 = 0.81$ , in consistent with the Planck 2018 results VI. Cosmological parameters.

EoR ( $z_{\text{em}} = z_{\text{re}}$ ),

$$P_x(k) = \frac{4\pi R^3}{3} e^{-k^2 R^2}, \quad (12)$$

where  $R$  is the characteristic radius of bubbles at  $z_{\text{re}}$ ,  $R \propto (1 + z_{\text{re}})^{-3/2}$  (Wyithe & Loeb 2004). However, this power spectrum is not realistic since  $P_x(k)$  should vanish when reionization ends ( $\bar{x}_{\text{HI}} \rightarrow 0$ ). Therefore, in this paper, we will not compare our results with toy model in Eq. (12).

A more realistic analytical model was given by Zaldarriaga et al. (2004) which also assumes randomly-distributed, single-size bubbles, but is not restricted to the end of the EoR, satisfying the constraint that  $P_x(k) \rightarrow 0$  when reionization finishes. In their model,

$$P_x(k) = (\sqrt{2\pi}R)^3 (\bar{x}_{\text{HI}} - \bar{x}_{\text{HI}}^2) e^{-k^2 R^2/2}. \quad (13)$$

In this paper, we will compare our simulation results with this analytical model (Eq. 13).

### 3.3. H I power spectrum and bias

In Figure 2, we illustrate the (equal-time) power spectrum of the H I density field,  $P_{\text{HI}}(k)$ , and that of the neutral fraction field,  $P_x(k)$ , both obtained from simulation data. The matter power spectrum is calculated using the CAMB package<sup>4</sup>. The simulated power spectra –  $P_{\text{HI}}(k)$ ,  $P_x(k)$ , and the cross-power  $P_{x_{\text{HI}}\delta}(k)$  – have similar shapes on all scales of interest, which indicates that the neutral fraction fluctuations dominate over the density fluctuations. For the purpose of a fair comparison between the simple analytical model and the seminumerical simulations, we set the characteristic bubble radius at the end of reionization in the toy model (Eq. 13) to be the photon horizon in the simulation, and take into account its growth during the EoR. On scales smaller than the characteristic bubble radius (sub-bubble scales), realistic  $P_x(k)$  from simulation shows a power-law-like decrease, slower than the exponential cutoff from the toy model. On scales larger than the characteristic bubble radius (super-bubble scales), however, the simulated power spectrum is smaller than the estimate from the toy model by nearly one order of magnitude. The reason is that at any fixed global ionized fraction during the EoR, realistic H II regions can have internal structures, whereas the toy model assumes fully ionized bubbles (two-phased IGM). Such a simplification would effectively transfer powers from sub-bubble scales to super-bubble scales.

Moreover, Figure 2 clearly shows that the neutral fraction and the matter overdensity field are anti-correlated,

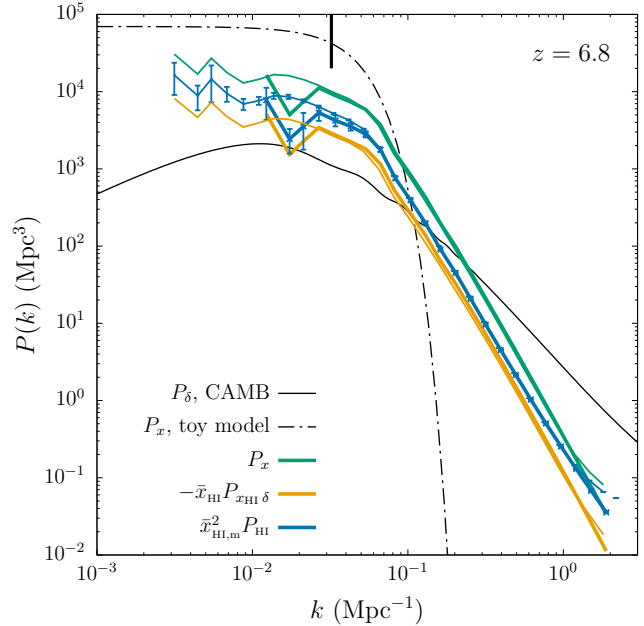


**Figure 2.** Power spectra of various sources at  $z = 6.8$  (corresponding to  $\bar{Q}_{\text{HI}} \approx 0.82$  in Model 1). Shown are the neutral fraction power spectrum  $P_x(k)$  (green solid line), the H I density power spectrum  $P_{\text{HI}}(k)$  (blue solid line), and the neutral fraction-density cross-power spectrum  $P_{x_{\text{HI}}\delta}(k)$  (yellow solid line), with the latter two power spectra being weighted by relevant factors. These power spectra are calculated from the seminumerical simulations of reionization in the small box (512 cMpc per side, thick colored lines), and in the large box (2000 cMpc per side, thin colored lines). The error bars on  $P_{\text{HI}}$  represent the sample variances corresponding to each simulation volume. For the purpose of comparison, we also show the matter power spectrum produced by CAMB (black solid line), and the neutral fraction power spectrum  $P_x(k)$  from the toy model using Eq. (13) (dot-dashed line) with the characteristic bubble radius in this toy model indicated by the black thick vertical line.

as a result of the inside-out reionization scenario. Also, their cross-power spectrum,  $P_{x_{\text{HI}}\delta}(k)$ , has comparable amplitude to  $P_x(k)$ , and hence is a non-negligible contribution to the 21 cm polarization power spectrum. Therefore, we include the cross-power ( $P_{\text{HI}}\delta(k)$  in our case) in our 21 cm signal modeling (Eqs. 6, 8 and 9).

In order to calculate the temperature and polarization anisotropy signals, we need relevant power spectra *on all scales*. To this end, it is useful to study the bias parameter,  $b_{\text{HI}}^2(k) \equiv P_{\text{HI}}(k)/P_\delta(k)$ , and  $b_{\text{HI},\times} \equiv P_{\text{HI}\delta}(k)/P_\delta(k)$ . We present in Figure 3 the simulated H I bias,  $b_{\text{HI}}^2$ , for all the reionization models in Table 1. (The bias from the cross-power  $b_{\text{HI},\times}$  agrees with  $b_{\text{HI}}(k)$  on large scales.) For the  $k$  range covered by simulations, we stitch together the results from the large and small boxes and discard data from  $k > 2 \text{ Mpc}^{-1}$ , to avoid the alias effect.

<sup>4</sup> <https://camb.info/>

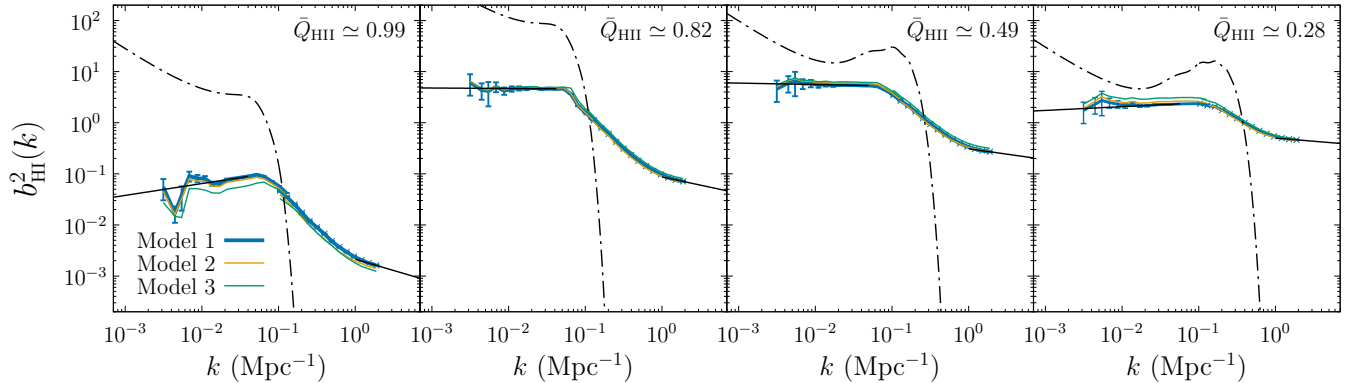


**Figure 3.** The H I bias at different ionized fractions during the EoR. Shown are the results from seminumerical reionization simulations for all three models in Table 1 (blue error bars representing the sample variance from Model 1), and those from the toy model (Eq. 13, dot-dashed lines). We extrapolate the bias from simulation with power-law fits (black solid lines) at both high and low ends of the  $k$  range beyond the simulation coverage.

Figure 3 shows that at a given global ionized fraction, the H I bias,  $b_{\text{HI}}^2(k)$ , is almost the same for all these models, regardless of the reionization parameters. As for its scale-dependence, since it is expected that the spatial distribution of the H I gas follows the underlying total matter on large scales, the H I bias should be constant on super-bubble scales throughout the EoR. Figure 3 confirms this point.<sup>5</sup> To accommodate the simulation results at all redshifts, we adopt a power-law extrapolation for the H I bias,  $b_{\text{HI}}^2(k) \propto k^n$ , on scales beyond either side of the simulation coverage. In contrast, the large-scale behavior of the H I bias from the toy model is very different, because its  $P_x(k)$  approaches constant as  $k \rightarrow 0$  in Eq. (13), resulting in a red-tilted  $b_{\text{HI}}^2(k)$ .

#### 4. RESULTS

We discuss the patterns and physical implications of the 21 cm TT, TE and EE power spectra with a fiducial model in §4.1, and focus on the evolution of  $C_\ell^{\text{TE}}$  and  $C_\ell^{\text{EE}}$  during the EoR and present their dependence on the global ionization history in §4.2.

##### 4.1. Generic feature of angular power spectra

While all the three models in Table 1 take reasonable reionization parameters and satisfy all current observational constraints, we choose Model 1 as the fiducial model just for illustration purpose. In Figure 4, we present its 21 cm temperature and polarization angular power spectrum at  $z_{\text{em}} = 6.8$  ( $\bar{Q}_{\text{HII}} \approx 0.82$ ). It shows that the temperature-polarization cross-power

spectrum,  $C_\ell^{\text{TE}}$ , is about four orders of magnitude smaller than the temperature power spectrum  $C_\ell^{\text{TT}}$ , and the polarization power spectrum  $C_\ell^{\text{EE}}$  is three orders of magnitude even smaller than  $C_\ell^{\text{TE}}$ . This will make the detection of 21 cm polarization signal very difficult, as we will see in §5. Regarding the comparison with the toy model, on the other hand, it shows that the toy model always underestimates the polarization (EE and TE) powers on small scales but overestimates them on large scales.

The EE power spectrum  $C_\ell^{\text{EE}}$  in Figure 4 shows a plateau on the intermediate angular scales and turns over at the scale of the typical bubble size ( $\ell \sim s/R$ ). The bump feature is caused by the turnover in the H I density power spectrum (see Figure 2). This feature due to the morphological structure of cosmic H II regions during the EoR is also reflected in  $C_\ell^{\text{TE}}$  at the angular scale of bubble size ( $\ell \sim s/R$ ), as shown in Figure 4.

On large scales, the temperature power spectrum turns out to be like a white noise, i.e.  $C_\ell^{\text{TT}} = \text{constant}$  for small  $\ell$  (Lewis & Challinor 2007). This is because for small  $\ell$  it is dominated by the contributions from the  $k$ -modes of small scales ( $ks > \ell$ ) rather than those of comparable scales. This is illustrated in Figure 5. While the temperature transfer function  $T_{\text{HI},\ell}^{\text{T}}(k)$  peaks near  $k_* \simeq \ell/s$ , the H I power spectrum peaks at much smaller scale. As a result, it turns out that the integrand of  $C_\ell^{\text{TT}}$  (see Eq. 8) peaks at a scale much smaller than  $k_*$  for small  $\ell$  (see the bottom panel of Figure 5). Given the shape of  $\Delta_{\text{HI}}^2(k)$ , only for large enough  $\ell$  ( $\ell \gtrsim 100$ ) does the majority of contributions to the  $C_\ell^{\text{TT}}$  integration come from the modes of comparable scales  $k_*$ .

However, this is not the case for the large-scale behavior of the temperature-polarization cross-power spectrum,  $C_\ell^{\text{TE}}$ , which involves the transfer function of the

<sup>5</sup> A caveat is the bias at the end of the EoR ( $\bar{Q}_{\text{HII}} \simeq 0.99$ ), as shown in the leftmost panel of Figure 3, showing a scale-dependence. This is likely a numerical artifact which arises because the seminumerical reionization simulation based on the excursion set model breaks down at that time.



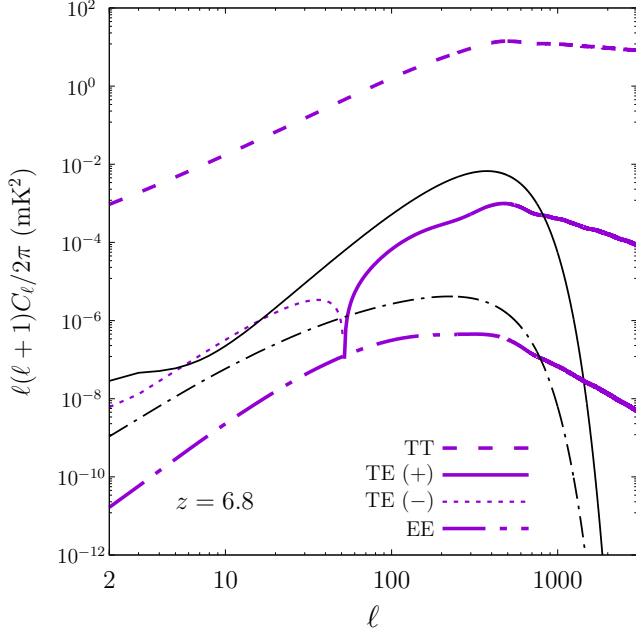


**Figure 4.** Angular power spectra of the 21 cm temperature (TT, dashed),  $E$ -mode polarization (EE, dot-dashed) and the temperature-polarization cross-correlation (TE, solid for positive part and dotted for negative part) at  $z_{\text{em}} = 6.8$  ( $\bar{Q}_{\text{HII}} \approx 0.82$ ). Shown are the results from the Model 1 of seminumerical simulation (purple lines), and from the toy model (Eq. 13, thin black lines). The TE power spectrum from simulation is plotted with its absolute value, with the dotted/solid line type marking the negative/positive part on the left/right-hand side of a sharp zero-crossing.

$E$ -mode polarization. Figure 6 shows that in  $C_\ell^{\text{TE}}$  the integration in Eq. (9) is always dominated by the modes near the characteristic scale  $k_* = \ell/s$ , for all  $\ell$ .

Furthermore, since  $T_{\text{HI},\ell}^{\text{T}} \mathcal{S}_{\text{HI},\ell}^{\text{E}}$  can be negative, as shown in Figure 6, the integrand of  $C_\ell^{\text{TE}}$  has negative parts, and those negative parts become more important as  $\ell$  is smaller. As a result, the integration over Fourier modes can result in negative values when  $\ell$  is small. This is why the  $C_\ell^{\text{TE}}$  from simulation results shows a zero-crossing at  $\ell < 100$ , as we find in Figure 4. However, the same figure also shows that  $C_\ell^{\text{TE}}$  from the toy model is always positive. This is because the toy model significantly overestimates the H I power spectrum at small  $k$  where  $T_{\text{HI},\ell}^{\text{T}}$  and  $\mathcal{S}_{\text{HI},\ell}^{\text{E}}$  are mostly positive, thereby enhancing the values of the integrand toward small  $k$ . This comparison between simulation and toy model results implies that the sign of  $C_\ell^{\text{TE}}$  is sensitive to the H I bias at large scales.

Specifically, we explore the impact of the large-scale scale-dependence of the H I bias on the zero-crossing angular scale of  $C_\ell^{\text{TE}}$ . For this purpose, we consider to extrapolate the H I bias at large scales as a constant,

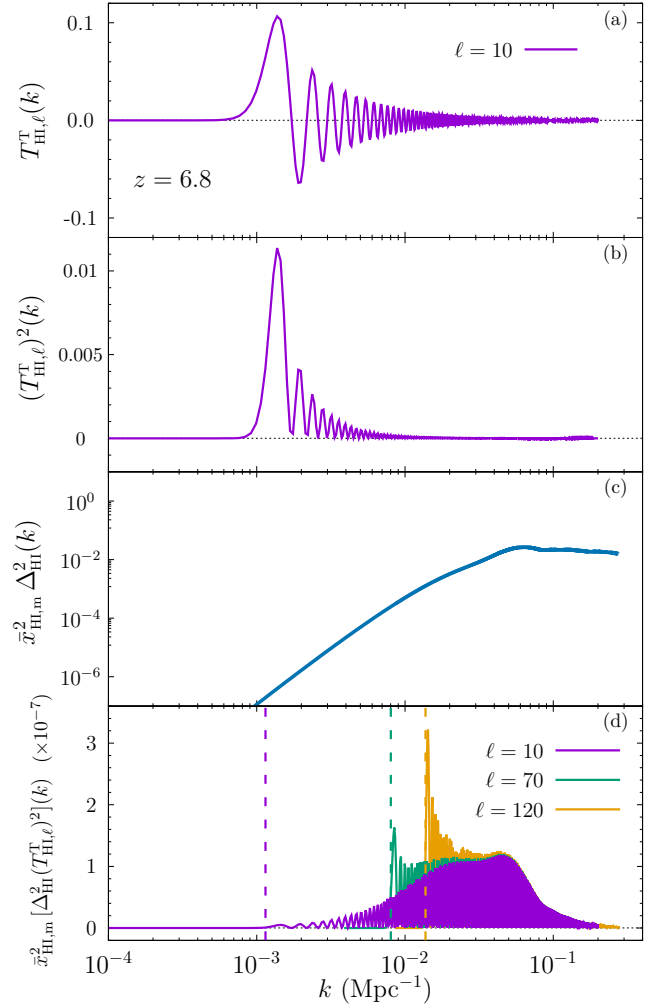


**Figure 5.** Contributions to the  $C_\ell^{\text{TT}}$  integration at  $z_{\text{em}} = 6.8$  in Model 1. (a) temperature transfer function of H I density fluctuations,  $T_{\text{HI},\ell}^{\text{T}}(k)$  with  $\ell = 10$ . (b)  $(T_{\text{HI},\ell}^{\text{T}})^2(k)$  with  $\ell = 10$ . (c) the dimensionless H I power spectrum,  $\Delta_{\text{HI}}^2(k) \equiv k^3 P_{\text{HI}}(k)/2\pi^2$ , weighted with relevant factor, from simulation. (Note that the power spectra at both high and low ends of the  $k$  range beyond the simulation coverage is obtained by extrapolating the H I bias from simulation with power-law fits.) (d) the leading term in the integrand of  $C_\ell^{\text{TT}}$  in Eq. (8),  $\bar{x}_{\text{HI},m}^2 \Delta_{\text{HI}}^2 (T_{\text{HI},\ell}^{\text{T}})^2$  (i.e. product of the quantities in (b) and (c)), as a function of wavenumber  $k$ , at various angular scales,  $\ell = 10/70/120$  (purple/green/yellow). The characteristic scale  $k_* = \ell/s$  at  $z_{\text{em}} = 6.8$  is indicated by the vertical lines for  $\ell$  of the same color.

instead of a power-law dependence. This difference is particularly significant for  $\bar{Q}_{\text{HII}} \simeq 0.99$  (see the leftmost panel of Figure 3). In Figure 7, we find that, for constant bias extrapolation, the zero-crossing angular scale evolves to larger angular scales as reionization proceeds, from  $\ell \sim 70$  at  $\bar{Q}_{\text{HII}} \simeq 0.28$  to  $\ell \sim 50$  at  $\bar{Q}_{\text{HII}} \simeq 0.99$ . Meanwhile, for a given  $\bar{Q}_{\text{HII}}$ , the change of the scale-

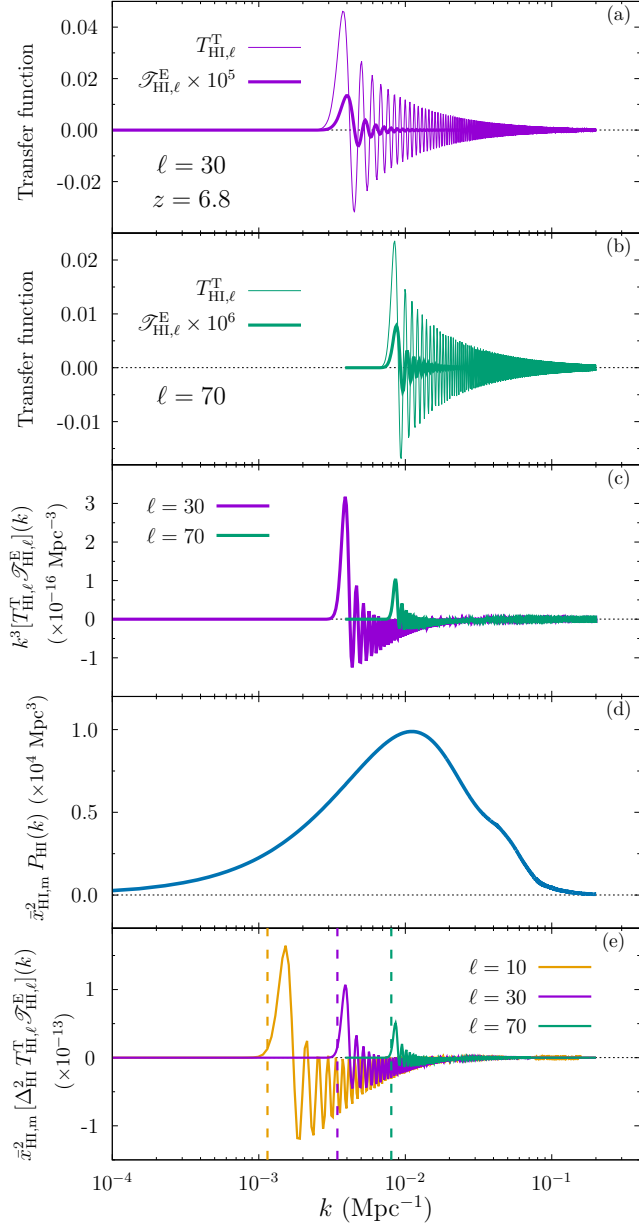


**Figure 6.** Contributions to the  $C_\ell^{\text{TE}}$  integration at  $z_{\text{em}} = 6.8$  in Model 1. (a) temperature and polarization transfer functions of H I density fluctuations  $T_{\text{HI},\ell}^{\text{T}}(k)$  (thin) and  $\mathcal{S}_{\text{HI},\ell}^{\text{E}}(k)$  (thick) at  $\ell = 30$ . (b) same as in (a) but for  $\ell = 70$ . (c)  $k^3 T_{\text{HI},\ell}^{\text{T}} \mathcal{S}_{\text{HI},\ell}^{\text{E}}$  for  $\ell = 30/70$  (purple/green). (d) H I density power spectrum  $P_{\text{HI}}(k)$ , multiplied by  $\bar{x}_{\text{HI},m}^2$  at this redshift. (e) the leading term in the integrand of  $C_\ell^{\text{TE}}$  in Eq. (9),  $\bar{x}_{\text{HI},m}^2 \Delta_{\text{HI}}^2 T_{\text{HI},\ell}^{\text{T}} \mathcal{S}_{\text{HI},\ell}^{\text{E}}$  as a function of wavenumber  $k$ , at various angular scales,  $\ell = 10/30/70$  (yellow/purple/green). The characteristic scale  $k_* = \ell/s$  at  $z_{\text{em}} = 6.8$  is indicated by the vertical lines for  $\ell$  of the same color.

dependence of the large-scale H I bias results in a shift of the zero-crossing angular scale. The explanation is that a linear H I bias effectively modulates the integrand with more weights on large scales than the bias with a positive power-law extrapolation, thus shifting the zero-crossing to a larger angular scale. Therefore, the zero-crossing feature in  $C_\ell^{\text{TE}}$  may be used to probe the *scale-dependence* of the H I bias during the EoR on super-bubble scales.

#### 4.2. Evolution and model-dependence

We plot the evolution of EE and TE power spectra, in Figures 8 and 9 respectively, at three representative angular scales corresponding to linear scales ( $\ell = 30$ ), the plateau (or the peak,  $\ell = 500$ ), and sub-bubble scales ( $\ell = 2000$ ). For both  $C_\ell^{\text{EE}}$  and  $C_\ell^{\text{TE}}$ , all curves exhibit a similar trend in the evolution of the amplitude of the signal: as reionization proceeds, the signal first rises to its peak and then gradually drops to almost zero when the IGM becomes fully ionized. The location of the peak is dependent on  $\ell$ , varying with a broad range  $\bar{Q}_{\text{HII}} \sim 0.50 - 0.70$ . The top panels of Figures 8 and 9 show that the powers at a given redshift are highly model-dependent. However, if we compare the powers *at a given global ionized fraction*  $\bar{Q}_{\text{HII}}$  from different models, we find that both the EE and TE powers display better convergence across these models in terms of their evolution trends (with small variations only).

Inspired by this finding, we plot the ratio  $C_\ell^{\text{EE}}/C_{\ell,\text{max}}^{\text{EE}}$  and  $C_\ell^{\text{TE}}/C_{\ell,\text{max}}^{\text{TE}}$  as function of  $\bar{Q}_{\text{HII}}$  in Figure 10, where  $C_{\ell,\text{max}}^{\text{EE}}$  ( $C_{\ell,\text{max}}^{\text{TE}}$ ) is the maximum value of  $C_\ell^{\text{EE}}$  ( $C_\ell^{\text{TE}}$ ) during the EoR at a given  $\ell$ . We find that the relations of these ratios and  $\bar{Q}_{\text{HII}}$  indeed display even better model-independence, for all three representative angular scales  $\ell$ . If 21 cm polarization measurement becomes technically achievable, then the robust mapping between the polarization signal and the global ionized fraction can be exploited to infer  $\bar{Q}_{\text{HII}}$  from the  $C_\ell^{\text{EE}}$  or  $C_\ell^{\text{TE}}$  measurements. This will help extract at least some part of the reionization history in later stages of the EoR.

Besides, Figure 10 shows that the full width at half maximum (FWHM) of the signal over the EoR is also insensitive to the ionization history, e.g. the FWHM of the power at  $\ell = 500$  approximately spans the range from  $\bar{Q}_{\text{HII}} = 0.50$  to  $0.90$ . In other words, once 21 cm polarization measurement becomes feasible, the polarization signal (analyzed using  $C_\ell^{\text{TE}}$  and  $C_\ell^{\text{EE}}$ ) from the EoR may be observed over a broad redshift (frequency) range —  $\Delta z \sim 1$  ( $\Delta\nu_{\text{obs}} \sim 30$  MHz) in terms of the FWHM — regardless of the global ionization history.

In short summary, our results show that the polarization of redshifted 21 cm lines can potentially probe large-

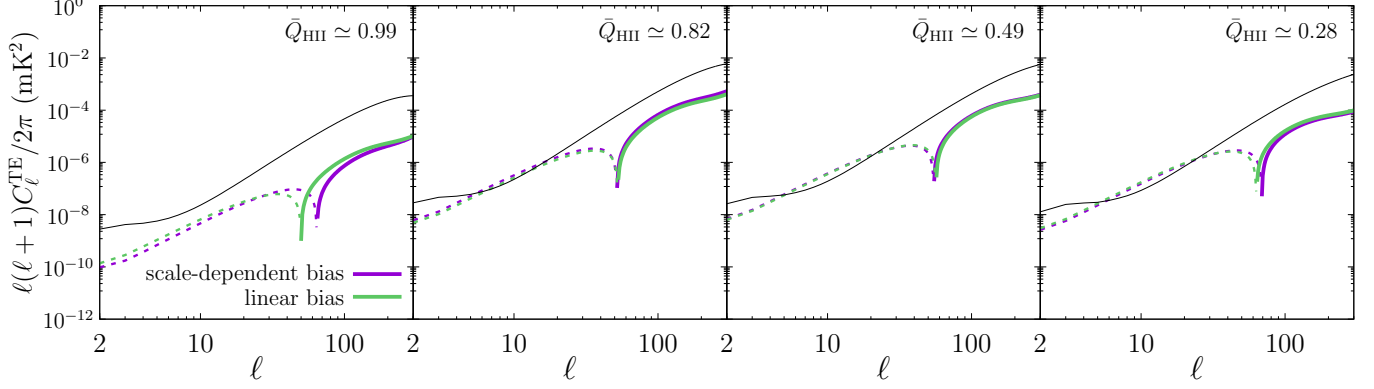


**Figure 7.** Large-scale TE angular power spectra at different ionized fractions during the EoR in seminumerical simulation Model 1 (colored lines) and in the toy model (Eq. 13, thin black lines).  $C_\ell^{\text{TE}}$  is plotted with its absolute value, with the dotted/solid line type marking the negative/positive part on the left/right-hand side of a sharp zero-crossing. For seminumerical simulations, shown are the results by employing a scale-dependent (power-law) extrapolation of the H I bias on large scales (purple lines), and by assuming a constant bias on large scales (green lines), respectively.

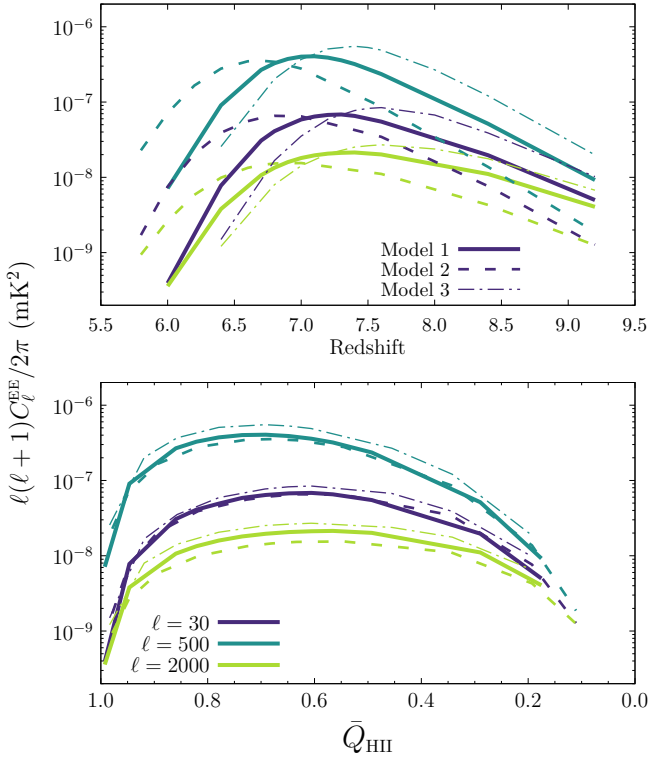


**Figure 8.** Evolution of the EE power spectrum  $C_\ell^{\text{EE}}$  at different angular scales  $\ell = 30/500/2000$  (purple/dark green/light green) during the EoR for different Model 1/2/3 (solid/dashed/dot-dashed line). (Top)  $C_\ell^{\text{EE}}$  as a function of redshift. (Bottom)  $C_\ell^{\text{EE}}$  as a function of the global H II volume filling fraction.

scale spatial fluctuations of neutral gas in the IGM, as well as the late-stage ionization history. In the next section we will discuss the prospects of its detection by upcoming intensity mapping experiments like SKA1-low.

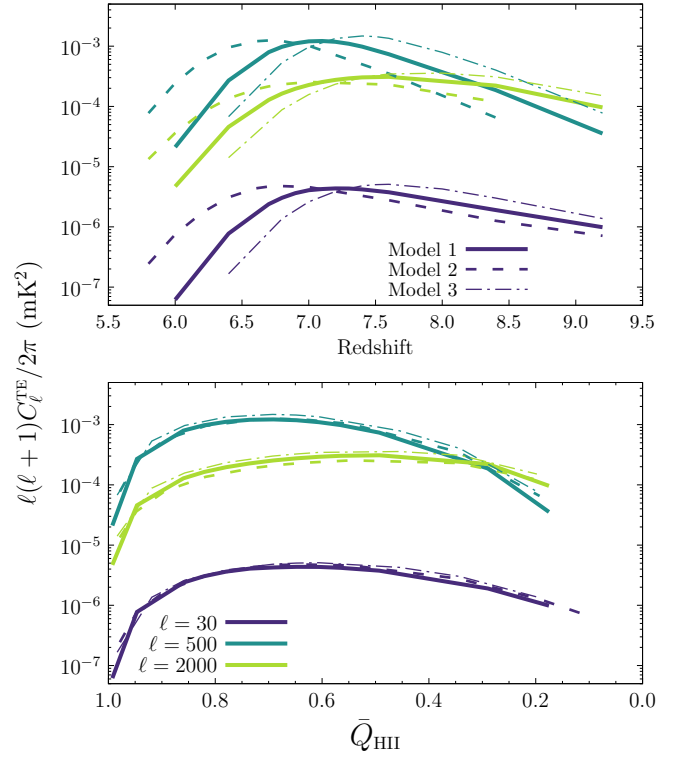


**Figure 9.** Same as Figure 8 but for the TE power spectrum  $C_\ell^{\text{TE}}$ . The results for  $\ell = 30$  are plotted with absolute values of  $C_\ell^{\text{TE}}$  since they are negative.

## 5. DETECTION PROSPECTS

While the temperature signal has hitherto been the focus of 21 cm cosmology, all Stokes parameters are actually often measured in intensity mapping surveys with low-frequency coverage (e.g., Shimwell et al. 2019; Riseley et al. 2020). In fact, polarization components have long been sought with a variety of science goals (see

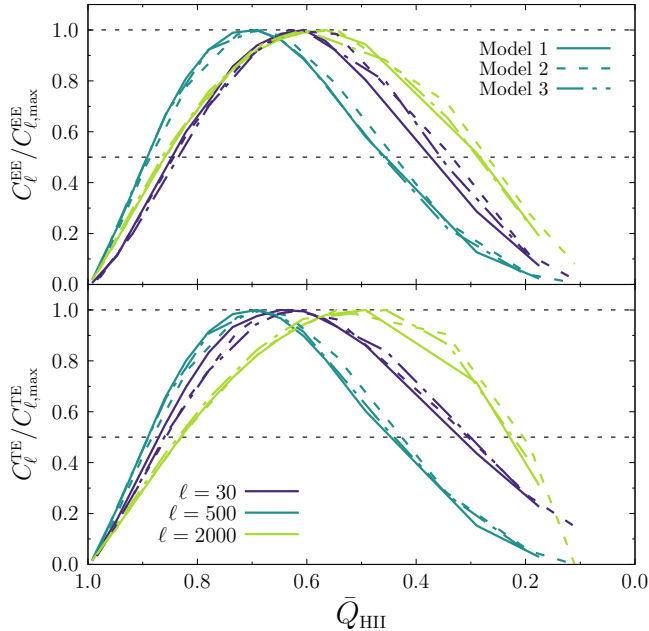


**Figure 10.** The ratio  $C_\ell^{\text{EE}}/C_{\ell,\text{max}}^{\text{EE}}$  (top) and  $C_\ell^{\text{TE}}/C_{\ell,\text{max}}^{\text{TE}}$  (bottom) as a function of the global H II volume filling fraction, for different Model 1/2/3 (solid/dashed/dot-dashed line) at different angular scales  $\ell = 30/500/2000$  (purple/dark green/light green). In the bottom panel, the ratios at  $\ell = 30$  are plotted with absolute values of  $C_\ell^{\text{TE}}$  since they are negative.

Heald et al. 2020, for a brief review), or for purposes of calibration and understanding instrumental systematics (e.g., Lenc et al. 2017; Gehlot et al. 2018).

Nevertheless, a practical measurement of the cosmological polarization signal from the EoR may be too ambitious a goal for current-generation experiments, due to several major challenges in 21 cm polarimetry — calibration (e.g., Sault et al. 1996; Bernardi et al. 2013; Kohn et al. 2019), foreground contamination from polarized diffuse synchrotron emission (Kogut et al. 2007; Lenc et al. 2016; Van Eck et al. 2019), instrumental leakage of intensity into polarization (e.g., Asad et al. 2018), the Faraday rotation effect which rotates the linear polarization by intervening magnetic fields of cosmic origins or in the ionosphere of the Earth (e.g., Jelić et al. 2010; Smirnov 2011; Moore et al. 2013), and depolarization effects (Burn 1966; Pratley & Johnston-Hollitt 2020).

Concerning these uncertainties, there have been continuous progresses in controlling the instrumental systematics and correcting for ionospheric activities to good levels, whereas the mitigation of radio foregrounds still seems a formidable task. For polarization, foreground mitigation is even more difficult than that for intensity, since both foregrounds and the 21 cm polarization signals are additionally subject to Faraday rotation, with

different Faraday depths along the LoS. Foreground subtraction algorithms, e.g.  $m$ -mode formalism (Shaw et al. 2014, 2015), and pseudo- $C_\ell$  algorithm (Alonso et al. 2019), as well as the foreground avoidance strategy (e.g., Datta et al. 2010; Morales et al. 2012; Liu et al. 2014), may provide efficient techniques for foreground mitigation. However, even if polarized foregrounds could be cleaned perfectly, Faraday rotation by the Galactic magnetic field alone can threaten the reconstruction of the cosmological linear polarization signal (De & Tashiro 2014).

On the bright side, Faraday rotation provides an avenue to study cosmic magnetic fields. By broadband observations and rotation measure (RM) synthesis techniques, modern radio astronomy aims at producing high precision RM maps which resolve structure of magnetic fields along each LoS (Heald 2015). As an example, an RM grid survey is planned on the SKA1-mid telescope (Johnston-Hollitt et al. 2015). Future magnetism science might then offer new approaches to separating polarized foregrounds and reconstructing the full Stokes parameters of the cosmological signal at the same time. Such a possibility is worth further scrutiny.

In this paper, we only demonstrate the detection sensitivity by the conventional estimate of the measurement noise—the rms noise fluctuation in the visibility of a fixed baseline in one frequency channel centered at  $\nu_{\text{obs},0}$  (Rohlf & Wilson 2004),

$$\Delta V^N = \frac{T_{\text{sys}}}{A_{\text{eff}}} \frac{\lambda_{\text{obs},0}^2}{\sqrt{\Delta\nu_{\text{obs},0} t_v}}, \quad (14)$$

where  $T_{\text{sys}}(\nu_{\text{obs},0})$  is the system temperature, which is the sum of the sky brightness temperature and the receiver temperature,  $A_{\text{eff}}$  is the effective collection area of one antenna/station,  $\Delta\nu_{\text{obs},0}$  is the bandwidth of the channel and  $t_v$  is the observation time in this channel.  $T_{\text{sys}}/A_{\text{eff}}$  characterizes the sensitivity of an antenna. In the case of SKA1-low, baselines are formed by pairs of stations and the zenith sensitivity within  $45^\circ$  for one station is  $A_{\text{eff}}/T_{\text{sys}} \approx 1.5 \text{ m}^2/\text{K}$  across relevant frequencies. Our assumption of sensitivity follows the SKA1-low antenna selection book<sup>6</sup>.

For illustration, we consider a drift-scan survey with maximal sky coverage by SKA1-low. Ignoring details of the map-making process in practice, we estimate the measurement uncertainty of  $C_\ell$  by the angular power spectrum of  $\Delta V^N$  (Zaldarriaga et al. 2004; Mondal et al.

<sup>6</sup> See the link at [SKA1\\_LOW\\_Antenna\\_Selection.pdf](#).

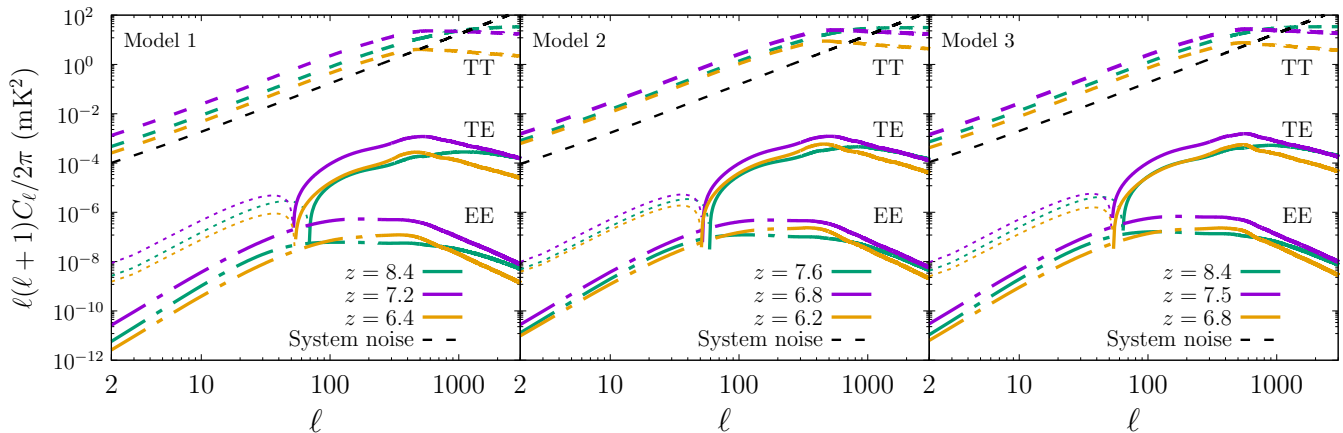


**Figure 11.** Angular power spectra of the 21 cm temperature (TT, dashed),  $E$ -mode polarization (EE, dot-dashed) and the temperature-polarization cross-correlation (TE, solid/dotted for the positive/negative part, respectively) from different Model 1/2/3 (left/middle/right panels). For each model (with different ionization history), shown are the results at various redshifts corresponding to  $\bar{Q}_{\text{HII}} \approx 0.35$  (green), 0.65 (purple) and 0.95 (yellow). TE power spectra are plotted with their absolute values, with the dotted/solid line type marking the negative/positive part on the left/right-hand side of a sharp zero-crossing. The black dashed line represents an estimate of the system noise of an SKA1-low survey with total observing time of 4096 hrs. The frequency band of the noise power spectrum corresponds to the redshift of the largest signal shown in each panel.

2020),

$$C_\ell^N \approx \frac{(2\pi)^2 (T_{\text{sys}}/A_{\text{eff}})^2 \lambda_{\text{obs},0}^2 A_{\text{total}}}{\Delta\nu_{\text{obs},0} t_0 2N_p N_s^2}, \quad (15)$$

where  $t_0$  is the total observing time,  $N_p = 2$  is the number of polarization states,  $A_{\text{total}}$  is the total area covered by the array and  $N_s$  is the number of stations within the array. Eq. (15) assumes a roughly uniform coverage of Fourier space during the course of the survey, preserving a white noise. For this reason, we only take into account the “core” of the actual SKA1-low array within the radius of about 500 meters, inside which 224 stations are closely packed<sup>7</sup>. We take the bandwidth to be  $\Delta\nu_{\text{obs},0} = 0.13$  MHz (2304 bands in total within the 50 – 350 MHz full SKA1-low bandwidth) and consider a total observing time of 4096 hrs (e.g., 512 nights with 8hrs per night).

The resulted noise power spectra are shown (labeled as “System noise”) in Figure 11. For comparison, we also plot the angular power spectra from different ionization histories. For each ionization history, the output redshifts are chosen such that they nearly correspond to  $\bar{Q}_{\text{HII}} \approx 0.35$ , 0.65 and 0.95. Although the error estimate here is primitive, the conclusion for  $C_\ell^{\text{TT}}$  is similar to that from Mondal et al. (2020) who accounted for the LC effect, that given reasonable integration time SKA1-low may detect the temperature signal by a signal-to-noise ratio (SNR) of over 10. However, for  $C_\ell^{\text{TE}}$  and

$C_\ell^{\text{EE}}$ , the 21 cm polarization signal is still several orders of magnitude below the noise power. This conclusion holds even if we relax the total observation time to  $t_0 = 20000$  hrs under the current design sensitivity of SKA1-low. It contrasts with the optimistic conclusion in BL05 because (1) the polarization signal from the EoR is overestimated at large scales in BL05, and (2) current design sensitivity of SKA1-low is much worse than the early illustration in BL05. Therefore, with the designed sensitivity of the current-generation interferometer array experiment, it is not feasible to measure the 21 cm polarization power spectrum.

## 6. SUMMARY

In this paper we reexamine the possibility of using the redshifted 21 cm polarization signal to probe cosmic reionization, in light of the upcoming H I intensity mapping surveys. For linearly polarized 21 cm lines due to Thomson scattering – the dominant mechanism for the 21 cm polarization signal – we improve the prediction of all-sky angular power spectra of the polarization autocorrelation and the temperature-polarization cross-correlation upon the previous work (BL05). We take into account the nonlinear effects due to inhomogeneous reionization, and perform realistic modeling of patchy reionization with seminumerical simulations.

We find that both power spectra  $C_\ell^{\text{EE}}$  and  $C_\ell^{\text{TE}}$  are enhanced on the sub-bubble (i.e. small) scales, compared to the previous predictions from BL05. On the large scales, however, the peak amplitudes of both power spectra, which correspond to the characteristic scale of bubbles, are smaller than the BL05 results. This is partly

<sup>7</sup> These parameters are adopted from the recent revision of the SKA1 baseline design document (SKA-TEL-SKO-0001075).

due to the fact that our formalism includes the anti-correlation between the matter density field and the neutral fraction field. In particular, for all the global ionization histories considered herein,  $\sqrt{\ell(\ell+1)C_{\ell,\max}^{\text{EE}}/2\pi}$  can only reach  $\sim 1\ \mu\text{K}$  and  $\sqrt{\ell(\ell+1)C_{\ell,\max}^{\text{TE}}/2\pi} \sim 0.03\ \text{mK}$ .

For the temperature-polarization cross-power spectrum, we find that  $C_{\ell}^{\text{TE}}$  displays a zero-crossing at  $\ell < 100$ , and its angular scale is sensitive to the scale-dependence of the large-scale H I bias during the EoR.

We demonstrate that the correlation between  $C_{\ell}/C_{\ell,\max}$  and the global ionized fraction  $\bar{Q}_{\text{HII}}$ , for both EE and TE power spectra, is robust against the variation of reionization parameters. This correlation may be exploited to infer the global ionized fraction from the measurement of  $C_{\ell}/C_{\ell,\max}$ , so as to reconstruct at least some part of the ionization history from the midpoint to the late stages of the EoR.

Regarding the detectability of the 21 cm polarization signal, the thermal noise, foregrounds and systematics remain challenges to the observations. Even with Faraday rotation corrected and foreground removed, the thermal noise in the polarization alone is still much larger than the signal in our new forecast, with the sensitivity of the SKA1-low telescope within reasonable integration time.

There still remains the possibility to probe the 21 cm polarization signal by its cross-correlation with other cosmic tracers (see Jelic et al. 2015 and references therein). For example, the cross-correlation of 21 cm polarization with the secondary CMB polarization due to patchy reionization (Doré et al. 2007) might be worth consideration since they are both generated by Thomson scattering off free electrons. Similar cross-correlation technique has been explored between 21 cm temperature and CMB kSZ signals (e.g., Cooray 2004; Alvarez et al. 2006).

## ACKNOWLEDGMENTS

This work is supported by National SKA Program of China (Grant No. 2020SKA0110401), NSFC (Grant No. 11821303), and National Key R&D Program of China (Grant No. 2018YFA0404502). We thank Shifan Zuo and Paulo Montero-Camacho for valuable comments and discussions, and thank the anonymous referee for constructive suggestions. Numerical evaluations and simulations in this work were ran at the Venus cluster at the Tsinghua University.

## APPENDIX

### A. THE 21 CM BASICS: RELATIVISTIC FORMALISM

This appendix contains the full relativistic formalism for the 21 cm signal from the EoR which we omit in §2.1 and leads to the starting point of our calculation, Eqs. (1) and (2). It closely follows those in Hall et al. (2013).

For the interest of this paper, the concept of observers extends to fictitious ones such as free electrons on the photon path. We consider such “observers” on the past light cone of the present-day Earth labeled by their *relative redshift*  $z_{\text{obs}}$  between the “observers” and the Earth today,  $1 + z_{\text{obs}} = \nu_{\text{obs}}/\nu_{\text{obs},0}$ , where  $\nu_{\text{obs}}$  and  $\nu_{\text{obs},0}$  are the radiation frequencies seen by the “observer” and on the Earth today, respectively. For a fixed observer, the location of 21 cm emission events is labeled by FLRW coordinates  $(t_{\text{em}}, \vec{x} + \vec{r})$ .  $\vec{x}$  is the location of the observer and  $\vec{r} \equiv -r\hat{n}$ .

The fundamental observable in 21 cm radiation for an “observer” is the differential 21 cm brightness temperature along a line of sight (LoS) per observed frequency

bin,  $\delta T_{\text{b}}(\nu_{\text{obs}}, \hat{n})$ , generally written as

$$\delta T_{\text{b}}(\nu_{\text{obs}}, \hat{n}) = \left[ \frac{T_{\text{s}}^g}{1+z} - T_{\text{CMB}}^{\text{obs}}(\hat{n}) \right] (1 - e^{-\tau_{\nu_{\text{obs}}}}), \quad (\text{A1})$$

where  $T_{\text{s}}^g$  is the spin temperature of the H I gas<sup>8</sup>,  $1+z = \nu_{21}/\nu_{\text{obs}}$  is the *relative redshift*<sup>9</sup> between the emission and the “observer”, and  $T_{\text{CMB}}^{\text{obs}}(\hat{n})$  is the CMB temperature along the LoS as seen by the “observer”.  $\nu_{21} = 1420\ \text{MHz}$  is the rest-frame frequency of the 21 cm transition.  $\tau_{\nu_{\text{obs}}}$  is the 21 cm optical depth at the observed frequency.

In Eq. (A1), the 21 cm optical depth is given by the LoS integration (e.g., Lewis & Challinor 2007),

$$\tau_{\nu_{\text{obs}}} = \int_{\text{em}}^{\text{obs}} \frac{3h^3 A_{10} n_{\text{HI}}^g T_{21}}{32\pi p^g T_{\text{s}}^g} \phi(E^g - E_{21}) d\lambda, \quad (\text{A2})$$

<sup>8</sup> In this paper, the superscript ‘g’ denotes quantities in the locally inertial rest frame of the emitting gas, and we assume single transition event along the LoS.

<sup>9</sup>  $z$  should not be confused with the cosmological redshift of the observer or that of the emitting gas in this paper.

where  $E^g = p^g c$  is the energy of the photon. The rest-frame 21 cm line profile  $\phi(E^g - E_{21})$  is defined such that  $\int \phi(E^g - E_{21}) dE^g = 1$ . It can be approximated as a Dirac delta function, hence simplifying the 21 cm optical depth:

$$\tau_{\nu_{\text{obs}}} = \frac{3h^3 c A_{10} T_{21} (1+z)}{32\pi E_{21}^2} \left( \frac{n_{\text{HI}}^g}{T_s^g} \left| \frac{d\lambda}{dz} \right| \right) \Big|_{\text{em}}, \quad (\text{A3})$$

where  $n_{\text{HI}}^g$  is the number density of the H I gas,  $\lambda$  is the affine parameter along the ray, and the subscript ‘em’ denotes the emission location where  $E^g(\lambda) = E_{21}$ . The (inverse) LoS differential redshift,  $|d\lambda/dz|$ , is attributed to the gravitational acceleration and the Doppler effect from the motion of the medium. It may diverge and thus cause  $\tau_{\nu_{\text{obs}}}$  to diverge, an extreme case due to the RSD component of the Doppler shift. However, for actual line profiles with finite width, the path integral in Eq. (A2) is always regular. Moreover, unlike the number count in galaxy redshift surveys, the brightness temperature given by Eq. (A1) is always finite even when  $\tau_{\nu_{\text{obs}}}$  diverges (Mao et al. 2012).

The relationship between the gauge-invariant (GI) observed redshift and the gauge-dependent cosmological redshift is that, to linear order,

$$\begin{aligned} (1+z) \frac{a(\eta_{\text{em}})}{a(\eta_{\text{obs}})} &= 1 + \hat{n} \cdot \left( \frac{\vec{v}_{\text{GI}}}{c} \right) \Big|_{\text{em}}^{\text{obs}} \\ &+ \left( \frac{\Psi_A}{c^2} + \frac{\Phi_H}{c^2} - \frac{\Phi}{c^2} + \frac{1}{3} \nabla^2 E \right) \Big|_{\text{em}}^{\text{obs}} \\ &- \int_{\text{em}}^{\text{obs}} \left( \frac{\dot{\Psi}_A}{c^2} + \frac{\dot{\Phi}_H}{c^2} - \frac{c}{a} n^i n^j \partial_i \dot{V}_j + \frac{1}{2} n^i n^j \dot{h}_{ij} \right) d\eta \\ &= 1 + \frac{\delta z}{1+z}, \end{aligned} \quad (\text{A4})$$

where the overdot denotes the partial time derivative with respect to  $\eta$ , the redshift variation  $\delta z \equiv 1+z - a(\eta_{\text{obs}})/a(\eta_{\text{em}})$ , and  $\Psi_A$ ,  $\Phi_H$ ,  $V_j$ ,  $h_{ij}$  are GI metric perturbations (Bardeen 1980; Bonvin & Durrer 2011). The GI velocity perturbation  $\vec{v}_{\text{GI}}$  is evaluated for both the observer and the emitting gas. It encodes the Doppler effect which sources the RSD.

In this paper, we adopt the conformal Newtonian gauge ( $B = E = 0$ ,  $\Psi = \Psi_A$ ,  $\Phi = \Phi_H$ ) and only considered scalar perturbations. We define a GI time variable, the cosmic time  $\bar{\eta}_{z_{\text{cos}}}$  which in the background FLRW model corresponds to cosmological redshift  $z_{\text{cos}}$ ,  $a(\bar{\eta}_{z_{\text{cos}}}) \equiv 1/(1+z_{\text{cos}})$ . We also assume that the H I gas is pressureless. Thus, according to the conservation of momentum,  $\dot{\vec{v}} + \mathcal{H} \vec{v} + \nabla \Psi = 0$ , where  $\vec{v}$  is the scalar-mode peculiar velocity of the gas.

### A.1. The 21 cm brightness temperature in the optically-thin, post-heating, quasi-linear regime

As described in §2.1, the working assumptions of this paper are listed as:  $\tau_{\nu_{\text{obs}}} \ll 1$ ,  $T_s^g(t_{\text{em}}) \gg (1+z)T_{\text{CMB}}^{\text{obs}}(\hat{n})$  and  $|\delta| \ll 1$ . Particularly, combining the optically-thin condition with Eq. (A3) implies that  $dz/d\lambda < 0$  along the ray with respect to the emitting gas, so that  $z(\lambda)$  is a monotonic function. As a result, the real-to-redshift-space coordinate conversion is always monotonic, i.e., no ‘‘Finger-of-God’’ effect for 21 cm radiation.

Plugging all the approximations and Eq. (A3) into Eq. (A1) yields the 21 cm brightness temperature for a fixed observer, to linear order,

$$\begin{aligned} \delta T_b(\eta_{\text{obs}}, \vec{x}, \nu_{\text{obs}}, \hat{n}) &\approx \frac{3h^3 c A_{10} T_{21} n_{\text{HI}}^g|_{\text{em}}}{32\pi E_{21}^2} \left| \frac{d\lambda}{dz} \right| \\ &\approx \frac{3c^3 A_{10} T_{21} n_{\text{HI}}^g|_{\text{em}}}{32\pi \nu_{21}^3 (1+z)} \left[ H(\eta) \left( 1 - \frac{\Psi}{c^2} \right) - \frac{1}{a} \frac{\dot{\Phi}}{c^2} \right. \\ &\quad \left. + \frac{1}{a} \hat{n} \cdot (\hat{n} \cdot \nabla \vec{v}) \right]^{-1} \Big|_{\text{em}} \\ &= \frac{3c^3 A_{10} T_{21} n_{\text{HI}}^g|_{\text{em}}}{32\pi \nu_{21}^3 (1+z) H(\eta_{\text{em}})} \left( 1 - \frac{\Psi}{c^2} - \frac{1}{\mathcal{H}} \frac{\dot{\Phi}}{c^2} \right. \\ &\quad \left. + \frac{1}{\mathcal{H}} \frac{\partial v_{\parallel}}{\partial r} \right)^{-1} \Big|_{\text{em}} \\ &\approx \frac{3c^3 A_{10} T_{21} \bar{n}_{\text{HI}}(\bar{\eta}_{z_{\text{em}}})}{32\pi \nu_{21}^3 (1+z) H(\bar{\eta}_{z_{\text{em}}})} \\ &\quad \times \frac{(1 + \delta_{\text{HI}}|_{\text{em}}) \left( 1 + \frac{\dot{\bar{n}}_{\text{HI}}(\bar{\eta}_{z_{\text{em}}})}{\bar{n}_{\text{HI}}(\bar{\eta}_{z_{\text{em}}})} \delta \eta_{\text{em}} \right)}{1 + \frac{\dot{H}}{H}(\bar{\eta}_{z_{\text{em}}}) \delta \eta_{\text{em}} + \left( \frac{1}{\mathcal{H}} \frac{\partial v_{\parallel}}{\partial r} - \frac{1}{\mathcal{H}} \frac{\dot{\Phi}}{c^2} - \frac{\Psi}{c^2} \right) \Big|_{\text{em}}} \end{aligned} \quad (\text{A5})$$

where  $n_{\text{HI}}|_{\text{em}} \equiv \bar{n}_{\text{HI}}(\eta_{\text{em}})(1 + \delta_{\text{HI}}|_{\text{em}})$  defines the fluctuations of H I distribution on the hypersurface of  $\eta_{\text{em}}$ <sup>10</sup>, and  $\delta \eta_{\text{em}} \equiv \eta_{\text{em}} - \bar{\eta}_{z_{\text{em}}}$ ,  $1 + z_{\text{em}} \equiv (1+z)(1+z_{\text{obs}}) = 1/\langle a(\eta_{\text{em}}) \rangle$ . The corresponding variation in the cosmological redshift can be defined as  $\delta z_{\text{em}} \equiv 1 + z_{\text{em}} - 1/a(\eta_{\text{em}})$ . We can show that  $\delta z_{\text{em}}/(1+z_{\text{em}}) = \mathcal{H}(z_{\text{em}}) \delta \eta_{\text{em}}$ . If the observer is on earth at the present,  $z_{\text{obs}} = 0$ ,  $z_{\text{em}} = z$  and  $\delta z_{\text{em}} = \delta z$ . Note that  $1 + z_{\text{em}} = \nu_{21}/\nu_{\text{obs},0}$ , even when the emission event is not on the past light cone of the present-day earth observer. Using Eq. (A4), we obtain the expression for the redshift

<sup>10</sup> Here instead of taking the H I number density in the gas rest frame, we take the value measured in the perturbed FLRW frame. The difference is second-order in  $|v|/c$  and thus negligible, so we work with this approximation throughout the paper.

variation in the Newtonian gauge,

$$\begin{aligned} \frac{\delta z_{\text{em}}}{1+z_{\text{em}}} &= \frac{\delta z}{1+z} + \frac{\delta z_{\text{obs}}}{1+z_{\text{obs}}} \\ &= \left( \hat{n} \cdot \frac{\vec{v}}{c} + \frac{\Psi}{c^2} \right) \Big|_{\text{em}}^0 - \left( \int_{\text{em}}^{\text{obs}} + \int_{\text{obs}}^0 \right) \left( \frac{\dot{\Psi}}{c^2} + \frac{\dot{\Phi}}{c^2} \right) d\eta, \\ \delta z_{\text{obs}} &\equiv z_{\text{obs}} - \tilde{z}_{\text{obs}}, \quad \langle \delta z_{\text{em}} \rangle = \langle \delta z \rangle = \langle \delta z_{\text{obs}} \rangle = 0, \\ \langle \delta \eta_{\text{em}} \rangle &= \langle \delta \eta_{\text{obs}} \rangle = 0. \end{aligned} \quad (\text{A6})$$

Eq. (A5) is the full relativistic expression for the 21 cm brightness temperature in the optically-thin, post-heating, quasi-linear limit, in agreement with Eq. (18) in Hall et al. (2013). The numerator and the denominator in the third line correspond to the redshift density perturbation ( $\delta_z$  in Bonvin & Durrer 2011) and the perturbation in the LoS length element extended by the gas per redshift bin ( $|d\lambda/dz|$ ), respectively, both GI. Note that the optically-thin limit is implied in the quasi-linear regime, since the RSD term (the velocity gradient) in the denominator is the only factor that can possibly make  $\tau_{\nu_{\text{obs}}}$  diverge. Eq. (A5) also shows that  $(1+z)\delta T_{\text{b}}$  is constant along the ray for fixed emission event and direction, as expected by the conservation of the photon distribution function during free streaming.

### A.2. The redshift-space expansion of the brightness temperature and peculiar velocity effects

21 cm photons seen by a fixed observer at a fixed redshift (Eq. [A1]) are actually emitted from different distances for different directions on the observer's past light cone. This is the so-called light-cone (LC) effect, mainly caused by the peculiar velocity of the gas. The extra anisotropy from the LC effect poses a major computational challenge to directly using Eq. (A5) to obtain the observed 21 cm signal. Also, it breaks the azimuthal symmetry around any mode vector  $\vec{k}$  in harmonic analysis, different from the CMB case. Besides the LC effect, H I peculiar velocities give rise to the RSD effect in the 21 cm intensity signal, as we see in Eq. (A5). The RSD occurs in the LoS length element,  $|d\lambda/dz|$ , as part of the Jacobian between the real- and redshift-space coordinates<sup>11</sup>. These effects need to be accounted for.

Our approximate solution is to rewrite the expression from the redshift-space point of view, by its Taylor expansion around the GI coordinate  $(\bar{\eta}_{z_{\text{em}}}, \vec{x} - s\hat{n})$ . It is the ensemble-averaged location of emission, as described in §2.1. The comoving radial distance in the redshift space

reads

$$\begin{aligned} s &\equiv \int_{z_{\text{obs}}}^{z_{\text{em}}} \frac{cd\tilde{z}}{H(\tilde{z})} = c(\bar{\eta}_{z_{\text{obs}}} - \bar{\eta}_{z_{\text{em}}}) = c\langle(\eta_{\text{obs}} - \eta_{\text{em}})\rangle \\ &= r(\hat{n}, z) + \frac{c\delta z_{\text{em}}}{H(z_{\text{em}})} - \frac{c\delta z_{\text{obs}}}{H(z_{\text{obs}})} = \langle r(\hat{n}, z) \rangle. \end{aligned} \quad (\text{A7})$$

Eq. (A6) shows that  $|\delta z|/(1+z) \ll 1$  for most of the emitting patches during the EoR, so that the Taylor series up to linear order of  $\delta\eta$  and  $(s-r)$  should be a good approximation for the signal. Discarding the negligible contribution from metric perturbations (the Sachs-Wolfe and integrated Sachs-Wolfe effect) in Eq. (A6) yields

$$\delta\eta_{\text{em}} \approx \frac{1}{\mathcal{H}(z_{\text{em}})} \frac{v_{\parallel}}{c} \Big|_0^{\text{em}}, \quad s-r \approx \frac{v_{\parallel}}{\mathcal{H}} \Big|_{\text{obs}}^{\text{em}}. \quad (\text{A8})$$

Throughout the paper we have dropped the contributions from the observer's site since they only affect the monopole and dipole of the observed anisotropy. Thus, we obtain the following expression for  $\Theta$  to linear order:

$$\begin{aligned} \Theta(\eta_{\text{obs}}, \vec{x}, \nu_{\text{obs}}, \hat{n}) &= \frac{n_{\text{HI}}|_{\text{em}}/\bar{n}_{\text{HI}}(z_{\text{em}})}{1 + \frac{\dot{H}}{H}(z_{\text{em}})\delta\eta_{\text{em}} + \left( \frac{1}{\mathcal{H}} \frac{\partial v_{\parallel}}{\partial r} - \frac{1}{\mathcal{H}} \frac{\dot{\Phi}}{c^2} - \frac{\Psi}{c^2} \right) \Big|_{\text{em}}} - 1 \\ &\approx \delta_{\text{HI}} - \frac{1}{\mathcal{H}} \frac{\partial v_{\parallel}}{\partial r} \frac{n_{\text{HI}}}{\bar{n}_{\text{HI}}} - (s-r) \frac{\partial \delta_{\text{HI}}}{\partial r} + \left( \frac{\dot{n}_{\text{HI}}}{\bar{n}_{\text{HI}}} - \frac{\dot{H}}{H} \frac{n_{\text{HI}}}{\bar{n}_{\text{HI}}} \right) \delta\eta_{\text{em}} \\ &\approx \delta_{\text{HI}} - \frac{1}{\mathcal{H}} \frac{\partial v_{\parallel}}{\partial r} \frac{n_{\text{HI}}}{\bar{n}_{\text{HI}}} - \frac{\partial \delta_{\text{HI}}}{\partial r} \frac{v_{\parallel}}{\mathcal{H}} \\ &\quad + \left[ \frac{\dot{n}_{\text{HI}}}{\bar{n}_{\text{HI}}} - \left( \frac{\dot{\mathcal{H}}}{\mathcal{H}} - \mathcal{H} \right) \frac{n_{\text{HI}}}{\bar{n}_{\text{HI}}} \right] \frac{v_{\parallel}}{c\mathcal{H}}, \end{aligned} \quad (\text{A9})$$

where all variables on the right-hand side of the last line above are evaluated at  $(\bar{\eta}_{z_{\text{em}}}, \vec{x} - s\hat{n})$ .

The expression above can be simplified using the conservation of hydrogen number,  $\dot{n}_{\text{H}} + \nabla \cdot (n_{\text{H}}\vec{v}) + 3(\mathcal{H} - \dot{\Phi}/c^2)n_{\text{H}} = 0$ , combined with the fact that  $n_{\text{HI}} = n_{\text{H}}x_{\text{HI}}$ . This leads to

$$\dot{n}_{\text{HI}} + \nabla \cdot (n_{\text{HI}}\vec{v}) + 3(\mathcal{H} - \dot{\Phi}/c^2)n_{\text{HI}} = \bar{n}_{\text{H}}(\dot{x}_{\text{HI}} + \nabla \cdot (x_{\text{HI}}\vec{v})). \quad (\text{A10})$$

Inserting it into Eq. (A9) yields

$$\begin{aligned} \Theta(\eta_{\text{obs}}, \vec{x}, \nu_{\text{obs}}, \hat{n}) &\approx \delta_{\text{HI}} - \frac{n_{\text{HI}}}{\bar{n}_{\text{HI}}} \frac{\partial_r v_{\parallel}}{\mathcal{H}} \\ &\quad + \left[ \frac{\dot{x}_{\text{HI}}}{\bar{x}_{\text{HI},\text{m}}} - \frac{c\partial_r n_{\text{HI}}}{\bar{n}_{\text{HI}}} - \left( \frac{\dot{\mathcal{H}}}{\mathcal{H}} + 2\mathcal{H} \right) \frac{n_{\text{HI}}}{\bar{n}_{\text{HI}}} \right] \frac{v_{\parallel}}{c\mathcal{H}}, \end{aligned} \quad (\text{A11})$$

where the second term on the right-hand side accounts for the RSD and the third term for the LC effect.

Figure 1 in Hall et al. (2013) shows that at low redshifts ( $z \sim 1-2$ ), the RSD is the dominant effect compared with the LC effect and metric perturbation terms

<sup>11</sup> The 1D distortion along the LoS in the intensity mapping case is thus distinct from the traditional RSD effect in galaxy surveys which occurs in the 3D volume element (Hall et al. 2013).



in the full expression (A5). In this paper we have also neglected the LC and relativistic effects for the EoR signal, only keeping the RSD term, though the former may cause a change of the signal by a factor of order unity (Chapman & Santos 2019).

### A.3. The resulting 21 cm brightness temperature

In Eq. (1), the dimensional factor  $T_0(z)$ , dependent on the relative redshift  $z$  between the emitter and the observer, is defined as

$$T_0(z) \equiv \frac{3c^3 A_{10} T_{21} \bar{n}_H(z_{\text{em}})}{32\pi\nu_{21}^3 (1+z) H(z_{\text{em}})}, \quad (\text{A12})$$

where  $A_{10} = 2.85 \times 10^{-15} \text{ s}^{-1}$  is the 21 cm spontaneous emission rate,  $T_{21} \equiv h\nu_{21}/k_B$ , and  $\bar{n}_H(z_{\text{em}}) = (3\Omega_b H_0^2 X_P / 8\pi G m_H) (1+z_{\text{em}})^3$ , ( $X_P$  is the cosmic hydrogen mass abundance and  $m_H$  is the mass of atomic hydrogen). The global 21 cm brightness temperature (the ensemble-averaged value of the monopole) is then given by

$$\begin{aligned} \delta\bar{T}_b(\nu_{\text{obs}}) &= T_0(z) \bar{x}_{\text{HI,m}}(z_{\text{em}}) = \frac{3c^3 A_{10} T_{21} \bar{n}_H(z_{\text{em}})}{32\pi\nu_{21}^3 (1+z) H(z_{\text{em}})} \\ &\approx (27\text{mK}) \left( \frac{\Omega_b h^2}{0.022} \right) \sqrt{\frac{0.14}{\Omega_m h^2} \frac{1+z_{\text{em}}}{10}} \bar{x}_{\text{HI,m}}(z_{\text{em}}). \end{aligned} \quad (\text{A13})$$

As for the fluctuation part, we work in the Fourier space for the temperature anisotropy  $\Theta$ , defined in §2.1. By definition,  $\Theta(\eta_{\text{obs}}, \vec{x}, \nu_{\text{obs}}, \hat{n}) = \delta T_b(\eta_{\text{obs}}, \vec{x}, \nu_{\text{obs}}, \hat{n}) / \delta\bar{T}_b(\nu_{\text{obs}}) - 1$ . Taking into account the linear-theory relation  $\vec{v}(\eta, \vec{k}) = i(\hat{k}/k) \mathcal{H}(\eta) \delta(\eta, \vec{k})$  during the matter-dominated era (Bharadwaj & Ali 2004), we obtain from Eq. (1) that

$$\begin{aligned} \Theta(\eta_{\text{obs}}, \vec{k}, \nu_{\text{obs}}, \hat{n}) &\approx \delta_{\text{HI}}(\vec{k}, z_{\text{em}}) e^{-i\mu ks} + \mu^2 \delta(\vec{k}, z_{\text{em}}) e^{-i\mu ks} \\ &+ \mathcal{C}_{\delta_{\text{HI}}\delta}(\vec{k}, z_{\text{em}}, \hat{n}) e^{-i\mu ks}, \end{aligned} \quad (\text{A14})$$

where the cross-term is  $\mathcal{C}_{\delta_{\text{HI}}\delta}(\vec{k}, z_{\text{em}}, \hat{n}) \equiv \int \frac{d^3\vec{k}'}{(2\pi)^3} \delta_{\text{HI}}(\vec{k} - \vec{k}') \delta(\vec{k}', (\hat{k}' \cdot \hat{n})^2)$ . The last two terms on the RHS of the equation above are due to the RSD, carrying intrinsic angular dependence (Hu & White 1997). Before and

during the early phase of reionization, the convolution  $\mathcal{C}_{\delta_{\text{HI}}\delta}$  is a second-order term so that the azimuthal symmetry around  $\vec{k}$  is preserved (Barkana & Loeb 2005; McQuinn et al. 2006). However, once  $\delta_{\text{HI}} \sim 1$ , the convolution term between the patchy H I field and the RSD may not be negligible even if the velocity field is still linear, breaking the azimuthal symmetry.

We leave the investigation of the convolution term to a future work and drop it in this paper. This assumption is valid at large scales where  $\delta_{\text{HI}} < 1$  still holds. Under this approximation,  $\Theta(\eta_{\text{obs}}, \vec{k}, \nu_{\text{obs}}, \hat{n}) = \Theta(\eta_{\text{obs}}, \vec{k}, \nu_{\text{obs}}, \mu)$ , i.e. its dependence on the LoS is only through functions of  $\mu$ . This yields the final expression, Eq. (2).

## B. GENERAL EXPRESSION FOR TEMPERATURE AND POLARIZATION ANGULAR POWER SPECTRA

In §2.2 we derive the angular power spectra of 21 cm temperature and polarization anisotropies, based on the expression for the temperature fluctuations given by Eq. (2), where  $\Theta$  is apparently sourced by  $\delta_{\text{HI}}$ , and  $\delta$  (via the RSD correction). However, as shown by Eq. (A9), other physical effects, e.g., the LC effect and relativistic metric perturbations, might affect the 21 cm radiation. For interested readers, here we present expressions for the general case in which multiple cosmological fields source temperature fluctuations and each source has its own transfer function. Those source fields are required to be statistically homogeneous and isotropic, and the temperature transfer functions should satisfy the azimuthal symmetry around  $\hat{k}$ . In other words,  $\Theta(\eta_{\text{obs}}, \vec{k}, \nu_{\text{obs}}, \mu) = \sum_i S_i(\vec{k}, z_{\text{em}}) T_i^{\text{T}}(\eta_{\text{obs}}, k, \nu_{\text{obs}}, \mu)$ , where  $S_i$  represent the initial conditions for the  $i$ -th source and  $T_i^{\text{T}}$  the temperature transfer functions.

The (equal-time) auto-power spectra and cross-power spectra of the initial source fields are given by  $\langle S_i^*(\vec{k}) S_i(\vec{k}') \rangle = (2\pi)^3 P_i(k) \delta_{\text{D}}^{(3)}(\vec{k} - \vec{k}')$  and  $\langle S_i^*(\vec{k}) S_j(\vec{k}') \rangle = (2\pi)^3 P_{ij}(k) \delta_{\text{D}}^{(3)}(\vec{k} - \vec{k}')$ . Also, for each source, we can define multipole moments of the temperature and polarization transfer functions,

$$T_{i,\ell}^{\text{T}}(\eta_{\text{obs}}, k, \nu_{\text{obs}}) \equiv \frac{1}{(-i)^\ell} \int_{-1}^1 \frac{d\mu}{2} \mathcal{P}_\ell(\mu) T_i^{\text{T}}(\eta_{\text{obs}}, k, \nu_{\text{obs}}, \mu), \quad (\text{B15})$$

$$\mathcal{F}_{i,\ell}^{\text{E}}(\eta_{\text{obs}}, k, \nu_{\text{obs}}) \equiv \frac{3}{4} \sqrt{\frac{(\ell+2)!}{(\ell-2)!}} \int_{\bar{\eta}_{z_{\text{em}}}}^{\bar{\eta}_{z_{\text{obs}}}} g(\eta') T_{i,2}^{\text{T}}(\eta', k, \nu') \frac{j_\ell[ck(\bar{\eta}_{z_{\text{obs}}} - \eta')]}{[ck(\bar{\eta}_{z_{\text{obs}}} - \eta')]^2} d\eta'. \quad (\text{B16})$$

Recall that  $1+z_{\text{em}} = (1+z)(1+z_{\text{obs}})$  and  $z$  is the observed (relative) redshift.

Hence, the angular power spectra of temperature and  $E$ -mode polarization anisotropies, for a generic observer located at  $(\eta_{\text{obs}}, \vec{x})$  and observing at frequency  $\nu_{\text{obs}}$ , are expressed as

$$C_{\ell}^{\text{EE}} = \frac{2}{\pi} \int k^2 dk \left[ \sum_i P_i(k, z_{\text{em}}) (\mathcal{T}_{i,\ell}^{\text{E}}(\eta_{\text{obs}}, k, \nu_{\text{obs}}))^2 + \sum_{i \neq j} P_{ij}(k, z_{\text{em}}) \mathcal{T}_{i,\ell}^{\text{E}}(\eta_{\text{obs}}, k, \nu_{\text{obs}}) \mathcal{T}_{j,\ell}^{\text{E}}(\eta_{\text{obs}}, k, \nu_{\text{obs}}) \right], \quad (\text{B17})$$

$$C_{\ell}^{\text{TT}} = \frac{2}{\pi} \int k^2 dk \left[ \sum_i P_i(k, z_{\text{em}}) (T_{i,\ell}(\eta_{\text{obs}}, k, \nu_{\text{obs}}))^2 + \sum_{i \neq j} P_{ij}(k, z_{\text{em}}) T_{i,\ell}(\eta_{\text{obs}}, k, \nu_{\text{obs}}) T_{j,\ell}(\eta_{\text{obs}}, k, \nu_{\text{obs}}) \right]. \quad (\text{B18})$$

The cross-power spectrum between the temperature and the  $E$ -mode polarization is

$$C_{\ell}^{\text{TE}} = \frac{2}{\pi} \int k^2 dk \left[ \sum_i P_i(k, z_{\text{em}}) T_{i,\ell}(\eta_{\text{obs}}, k, \nu_{\text{obs}}) \mathcal{T}_{i,\ell}^{\text{E}}(\eta_{\text{obs}}, k, \nu_{\text{obs}}) + \sum_{i \neq j} P_{ij}(k, z_{\text{em}}) T_{i,\ell}(\eta_{\text{obs}}, k, \nu_{\text{obs}}) \mathcal{T}_{j,\ell}^{\text{E}}(\eta_{\text{obs}}, k, \nu_{\text{obs}}) \right]. \quad (\text{B19})$$

---

### C. PREVIOUS MODELING OF THE 21 CM POLARIZATION

Following Eq. (11) and the standard procedure, the formulae of 21 cm polarization angular power spectra in BL05 (their Eqs. 13 and 25) can be rewritten using *our* notation<sup>12</sup> as

$$C_{\ell}^{\text{EE}} = \frac{2}{\pi} \int k^2 dk \left\{ [\bar{x}_{\text{HI}}^{-2} P_x(k) + P_{\delta}(k)] (\mathcal{T}_{\text{HI},\ell}^{\text{E}}(k))^2 + P_{\delta}(k) (\mathcal{T}_{\delta,\ell}^{\text{E}}(k))^2 + 2 P_{\delta}(k) \mathcal{T}_{\text{HI},\ell}^{\text{E}}(k) \mathcal{T}_{\delta,\ell}^{\text{E}}(k) \right\}, \quad (\text{C20})$$

$$C_{\ell}^{\text{TE}} = \frac{2}{\pi} \int k^2 dk \left\{ [\bar{x}_{\text{HI}}^{-2} P_x(k) + P_{\delta}(k)] T_{\text{HI},\ell}^{\text{T}}(k) \mathcal{T}_{\text{HI},\ell}^{\text{E}}(k) + P_{\delta}(k) T_{\delta,\ell}^{\text{T}}(k) \mathcal{T}_{\delta,\ell}^{\text{E}}(k) + P_{\delta}(k) [T_{\text{HI},\ell}^{\text{T}}(k) \mathcal{T}_{\delta,\ell}^{\text{E}}(k) + T_{\delta,\ell}^{\text{T}}(k) \mathcal{T}_{\text{HI},\ell}^{\text{E}}(k)] \right\}, \quad (\text{C21})$$

where, again, all the transfer functions are evaluated at  $(\eta_0, \nu_{\text{obs},0})$ , all the power spectra and  $\bar{x}_{\text{HI}}$  are evaluated at  $z_{\text{em}}$ , and the dimensional results should be obtained by multiplying the extra factor of  $[T_0(z_{\text{em}}) \bar{x}_{\text{HI},\text{m}}(z_{\text{em}})]^2$ .

Comparing Eqs. (C20) and (C21) with Eqs. (6) and (9), it is realized that the approximations made in BL05 are  $P_{\text{HI}}(k) \approx \bar{x}_{\text{HI}}^{-2} P_x(k) + P_{\delta}(k)$  and  $P_{\text{HI}\delta}(k) \approx P_{\delta}(k)$ . Since  $\delta_{\text{HI}} = \delta x_{\text{HI}} + \delta + \delta x_{\text{HI}} \delta$ , we have  $P_{\text{HI}}(k) =$

$\bar{x}_{\text{HI}}^{-2} P_x(k) + P_{\delta}(k) + 2\bar{x}_{\text{HI}}^{-1} P_{x_{\text{HI}}\delta} +$  (higher-order cross terms), and  $P_{\text{HI}\delta}(k) = P_{\delta}(k) + \bar{x}_{\text{HI}}^{-1} P_{x_{\text{HI}}\delta} +$  (higher-order cross terms). Therefore, not only did BL05 ignore the higher-order cross terms due to  $\delta x_{\text{HI}} \delta$ , but also it ignored the leading-order cross term  $P_{x_{\text{HI}}\delta}$ . In comparison, our formalism is expanded on the H I density fluctuations, which automatically corrects for both issues.

---

### REFERENCES

- Ahn, K., Xu, H., Norman, M. L., Alvarez, M. A., & Wise, J. H. 2015, *ApJ*, 802, 8, doi: [10.1088/0004-637X/802/1/8](https://doi.org/10.1088/0004-637X/802/1/8)
- Alonso, D., Sanchez, J., Slosar, A., & LSST Dark Energy Science Collaboration. 2019, *MNRAS*, 484, 4127, doi: [10.1093/mnras/stz093](https://doi.org/10.1093/mnras/stz093)
- Alvarez, M. A., Komatsu, E., Doré, O., & Shapiro, P. R. 2006, *ApJ*, 647, 840, doi: [10.1086/504888](https://doi.org/10.1086/504888)
- Asad, K. M. B., Koopmans, L. V. E., Jelić, V., et al. 2018, *MNRAS*, 476, 3051, doi: [10.1093/mnras/sty258](https://doi.org/10.1093/mnras/sty258)

<sup>12</sup> Note that in BL05, the multipole moments of the transfer functions due to the RSD,  $T_{\delta,\ell}^{\text{T}}$  and  $\mathcal{T}_{\delta,\ell}^{\text{E}}$ , take different forms from ours. This can be understood by comparing Eq. (3) with Eq. (11).

- Babich, D., & Loeb, A. 2005, *ApJ*, 635, 1, doi: [10.1086/497297](https://doi.org/10.1086/497297)
- Baek, S., Di Matteo, P., Semelin, B., Combes, F., & Revaz, Y. 2009, *A&A*, 495, 389, doi: [10.1051/0004-6361:200810757](https://doi.org/10.1051/0004-6361:200810757)
- Baek, S., Semelin, B., Di Matteo, P., Revaz, Y., & Combes, F. 2010, *A&A*, 523, A4, doi: [10.1051/0004-6361/201014347](https://doi.org/10.1051/0004-6361/201014347)
- Bardeen, J. M. 1980, *PhRvD*, 22, 1882, doi: [10.1103/PhysRevD.22.1882](https://doi.org/10.1103/PhysRevD.22.1882)
- Barkana, R., & Loeb, A. 2001, *PhR*, 349, 125, doi: [10.1016/S0370-1573\(01\)00019-9](https://doi.org/10.1016/S0370-1573(01)00019-9)
- . 2005, *ApJL*, 624, L65, doi: [10.1086/430599](https://doi.org/10.1086/430599)
- . 2006, *MNRAS*, 372, L43, doi: [10.1111/j.1745-3933.2006.00222.x](https://doi.org/10.1111/j.1745-3933.2006.00222.x)
- Battaglia, N., Trac, H., Cen, R., & Loeb, A. 2013, *ApJ*, 776, 81, doi: [10.1088/0004-637X/776/2/81](https://doi.org/10.1088/0004-637X/776/2/81)
- Becker, G. D., Bolton, J. S., Madau, P., et al. 2015, *MNRAS*, 447, 3402, doi: [10.1093/mnras/stu2646](https://doi.org/10.1093/mnras/stu2646)
- Bernardi, G., Greenhill, L. J., Mitchell, D. A., et al. 2013, *ApJ*, 771, 105, doi: [10.1088/0004-637X/771/2/105](https://doi.org/10.1088/0004-637X/771/2/105)
- Bharadwaj, S., & Ali, S. S. 2004, *MNRAS*, 352, 142, doi: [10.1111/j.1365-2966.2004.07907.x](https://doi.org/10.1111/j.1365-2966.2004.07907.x)
- Bonvin, C., & Durrer, R. 2011, *PhRvD*, 84, 063505, doi: [10.1103/PhysRevD.84.063505](https://doi.org/10.1103/PhysRevD.84.063505)
- Bouwens, R. J., Illingworth, G. D., Oesch, P. A., et al. 2015, *ApJ*, 811, 140, doi: [10.1088/0004-637X/811/2/140](https://doi.org/10.1088/0004-637X/811/2/140)
- Burn, B. J. 1966, *MNRAS*, 133, 67, doi: [10.1093/mnras/133.1.67](https://doi.org/10.1093/mnras/133.1.67)
- Chapman, E., & Santos, M. G. 2019, *MNRAS*, 490, 1255, doi: [10.1093/mnras/stz2663](https://doi.org/10.1093/mnras/stz2663)
- Chen, X., & Miralda-Escudé, J. 2004, *ApJ*, 602, 1, doi: [10.1086/380829](https://doi.org/10.1086/380829)
- Chen, Z., Xu, Y., Wang, Y., & Chen, X. 2019, *ApJ*, 885, 23, doi: [10.3847/1538-4357/ab43e6](https://doi.org/10.3847/1538-4357/ab43e6)
- Cooray, A. 2004, *PhRvD*, 70, 063509, doi: [10.1103/PhysRevD.70.063509](https://doi.org/10.1103/PhysRevD.70.063509)
- Cooray, A., & Furlanetto, S. R. 2005, *MNRAS*, 359, L47, doi: [10.1111/j.1745-3933.2005.00035.x](https://doi.org/10.1111/j.1745-3933.2005.00035.x)
- Datta, A., Bowman, J. D., & Carilli, C. L. 2010, *ApJ*, 724, 526, doi: [10.1088/0004-637X/724/1/526](https://doi.org/10.1088/0004-637X/724/1/526)
- Datta, K. K., Choudhury, T. R., & Bharadwaj, S. 2007, *MNRAS*, 378, 119, doi: [10.1111/j.1365-2966.2007.11747.x](https://doi.org/10.1111/j.1365-2966.2007.11747.x)
- Dayal, P., & Ferrara, A. 2018, *PhR*, 780, 1, doi: [10.1016/j.physrep.2018.10.002](https://doi.org/10.1016/j.physrep.2018.10.002)
- De, S., & Tashiro, H. 2014, *PhRvD*, 89, 123002, doi: [10.1103/PhysRevD.89.123002](https://doi.org/10.1103/PhysRevD.89.123002)
- DeBoer, D. R., Parsons, A. R., Aguirre, J. E., et al. 2017, *PASP*, 129, 045001, doi: [10.1088/1538-3873/129/974/045001](https://doi.org/10.1088/1538-3873/129/974/045001)
- Dixon, K. L., Iliev, I. T., Mellema, G., Ahn, K., & Shapiro, P. R. 2016, *MNRAS*, 456, 3011, doi: [10.1093/mnras/stv2887](https://doi.org/10.1093/mnras/stv2887)
- Doré, O., Holder, G., Alvarez, M., et al. 2007, *PhRvD*, 76, 043002, doi: [10.1103/PhysRevD.76.043002](https://doi.org/10.1103/PhysRevD.76.043002)
- Fan, X., Strauss, M. A., Becker, R. H., et al. 2006, *AJ*, 132, 117, doi: [10.1086/504836](https://doi.org/10.1086/504836)
- Finkelstein, S. L., D'Aloisio, A., Paardekooper, J.-P., et al. 2019, *ApJ*, 879, 36, doi: [10.3847/1538-4357/ab1ea8](https://doi.org/10.3847/1538-4357/ab1ea8)
- Furlanetto, S. R. 2006, *MNRAS*, 371, 867, doi: [10.1111/j.1365-2966.2006.10725.x](https://doi.org/10.1111/j.1365-2966.2006.10725.x)
- Furlanetto, S. R., Zaldarriaga, M., & Hernquist, L. 2004a, *ApJ*, 613, 16, doi: [10.1086/423028](https://doi.org/10.1086/423028)
- . 2004b, *ApJ*, 613, 1, doi: [10.1086/423025](https://doi.org/10.1086/423025)
- Gehlot, B. K., Koopmans, L. V. E., de Bruyn, A. G., et al. 2018, *MNRAS*, 478, 1484, doi: [10.1093/mnras/sty1095](https://doi.org/10.1093/mnras/sty1095)
- Greig, B., & Mesinger, A. 2017, *MNRAS*, 465, 4838, doi: [10.1093/mnras/stw3026](https://doi.org/10.1093/mnras/stw3026)
- . 2018, *MNRAS*, 477, 3217, doi: [10.1093/mnras/sty796](https://doi.org/10.1093/mnras/sty796)
- Greig, B., Mesinger, A., Haiman, Z., & Simcoe, R. A. 2017, *MNRAS*, 466, 4239, doi: [10.1093/mnras/stw3351](https://doi.org/10.1093/mnras/stw3351)
- Gruzinov, A., & Hu, W. 1998, *ApJ*, 508, 435, doi: [10.1086/306432](https://doi.org/10.1086/306432)
- Hall, A., Bonvin, C., & Challinor, A. 2013, *PhRvD*, 87, 064026, doi: [10.1103/PhysRevD.87.064026](https://doi.org/10.1103/PhysRevD.87.064026)
- Heald, G. 2015, *Astrophysics and Space Science Library*, Vol. 407, Synchrotron Radiation and Faraday Rotation, ed. A. Lazarian, E. M. de Gouveia Dal Pino, & C. Melioli, 41, doi: [10.1007/978-3-662-44625-6\\_3](https://doi.org/10.1007/978-3-662-44625-6_3)
- Heald, G., Mao, S., Vacca, V., et al. 2020, *Galaxies*, 8, 53, doi: [10.3390/galaxies8030053](https://doi.org/10.3390/galaxies8030053)
- Hirata, C. M., Mishra, A., & Venumadhav, T. 2018, *PhRvD*, 97, 103521, doi: [10.1103/PhysRevD.97.103521](https://doi.org/10.1103/PhysRevD.97.103521)
- Hoffmann, K., Mao, Y., Xu, J., Mo, H., & Wandelt, B. D. 2019, *MNRAS*, 487, 3050, doi: [10.1093/mnras/stz1472](https://doi.org/10.1093/mnras/stz1472)
- Hu, W. 2000, *ApJ*, 529, 12, doi: [10.1086/308279](https://doi.org/10.1086/308279)
- Hu, W., & Sugiyama, N. 1995, *ApJ*, 444, 489, doi: [10.1086/175624](https://doi.org/10.1086/175624)
- Hu, W., & White, M. 1997, *PhRvD*, 56, 596, doi: [10.1103/PhysRevD.56.596](https://doi.org/10.1103/PhysRevD.56.596)
- Hutter, A. 2018, *MNRAS*, 477, 1549, doi: [10.1093/mnras/sty683](https://doi.org/10.1093/mnras/sty683)
- Iliev, I. T., Mellema, G., Ahn, K., et al. 2014, *MNRAS*, 439, 725, doi: [10.1093/mnras/stt2497](https://doi.org/10.1093/mnras/stt2497)
- Iliev, I. T., Mellema, G., Pen, U. L., et al. 2006, *MNRAS*, 369, 1625, doi: [10.1111/j.1365-2966.2006.10502.x](https://doi.org/10.1111/j.1365-2966.2006.10502.x)
- Intema, H. T., Jagannathan, P., Mooley, K. P., & Frail, D. A. 2017, *A&A*, 598, A78, doi: [10.1051/0004-6361/201628536](https://doi.org/10.1051/0004-6361/201628536)

- Jelic, V., Ciardi, B., Fernandez, E., Tashiro, H., & Vrbanec, D. 2015, in *Advancing Astrophysics with the Square Kilometre Array (AASKA14)*, 8. <https://arxiv.org/abs/1501.04247>
- Jelić, V., Zaroubi, S., Labropoulos, P., et al. 2010, *MNRAS*, 409, 1647, doi: [10.1111/j.1365-2966.2010.17407.x](https://doi.org/10.1111/j.1365-2966.2010.17407.x)
- Ji, L., Kamionkowski, M., & Inomata, K. 2021, *PhRvD*, 103, 023516, doi: [10.1103/PhysRevD.103.023516](https://doi.org/10.1103/PhysRevD.103.023516)
- Johnston-Hollitt, M., Govoni, F., Beck, R., et al. 2015, in *Advancing Astrophysics with the Square Kilometre Array (AASKA14)*, 92. <https://arxiv.org/abs/1506.00808>
- Knox, L., Scoccamarro, R., & Dodelson, S. 1998, *PhRvL*, 81, 2004, doi: [10.1103/PhysRevLett.81.2004](https://doi.org/10.1103/PhysRevLett.81.2004)
- Kogut, A., Dunkley, J., Bennett, C. L., et al. 2007, *ApJ*, 665, 355, doi: [10.1086/519754](https://doi.org/10.1086/519754)
- Kohn, S. A., Aguirre, J. E., La Plante, P., et al. 2019, *ApJ*, 882, 58, doi: [10.3847/1538-4357/ab2f72](https://doi.org/10.3847/1538-4357/ab2f72)
- Koopmans, L., Pritchard, J., Mellema, G., et al. 2015, in *Advancing Astrophysics with the Square Kilometre Array (AASKA14)*, 1. <https://arxiv.org/abs/1505.07568>
- Lenc, E., Gaensler, B. M., Sun, X. H., et al. 2016, *ApJ*, 830, 38, doi: [10.3847/0004-637X/830/1/38](https://doi.org/10.3847/0004-637X/830/1/38)
- Lenc, E., Anderson, C. S., Barry, N., et al. 2017, *PASA*, 34, e040, doi: [10.1017/pasa.2017.36](https://doi.org/10.1017/pasa.2017.36)
- Lewis, A., & Challinor, A. 2007, *PhRvD*, 76, 083005, doi: [10.1103/PhysRevD.76.083005](https://doi.org/10.1103/PhysRevD.76.083005)
- Lidz, A., Zahn, O., McQuinn, M., Zaldarriaga, M., & Hernquist, L. 2008, *ApJ*, 680, 962, doi: [10.1086/587618](https://doi.org/10.1086/587618)
- Liu, A., Parsons, A. R., & Trott, C. M. 2014, *PhRvD*, 90, 023018, doi: [10.1103/PhysRevD.90.023018](https://doi.org/10.1103/PhysRevD.90.023018)
- Liu, A., & Shaw, J. R. 2020, *PASP*, 132, 062001, doi: [10.1088/1538-3873/ab5bfd](https://doi.org/10.1088/1538-3873/ab5bfd)
- Liu, A., Zhang, Y., & Parsons, A. R. 2016, *ApJ*, 833, 242, doi: [10.3847/1538-4357/833/2/242](https://doi.org/10.3847/1538-4357/833/2/242)
- Madau, P., Meiksin, A., & Rees, M. J. 1997, *ApJ*, 475, 429, doi: [10.1086/303549](https://doi.org/10.1086/303549)
- Majumdar, S., Mellema, G., Datta, K. K., et al. 2014, *MNRAS*, 443, 2843, doi: [10.1093/mnras/stu1342](https://doi.org/10.1093/mnras/stu1342)
- Mao, Y., Koda, J., Shapiro, P. R., et al. 2020, *MNRAS*, 491, 1600, doi: [10.1093/mnras/stz2986](https://doi.org/10.1093/mnras/stz2986)
- Mao, Y., Shapiro, P. R., Mellema, G., et al. 2012, *MNRAS*, 422, 926, doi: [10.1111/j.1365-2966.2012.20471.x](https://doi.org/10.1111/j.1365-2966.2012.20471.x)
- Mao, Y., Tegmark, M., McQuinn, M., Zaldarriaga, M., & Zahn, O. 2008, *PhRvD*, 78, 023529, doi: [10.1103/PhysRevD.78.023529](https://doi.org/10.1103/PhysRevD.78.023529)
- McGreer, I. D., Mesinger, A., & D'Odorico, V. 2015, *MNRAS*, 447, 499, doi: [10.1093/mnras/stu2449](https://doi.org/10.1093/mnras/stu2449)
- McQuinn, M., Lidz, A., Zahn, O., et al. 2007, *MNRAS*, 377, 1043, doi: [10.1111/j.1365-2966.2007.11489.x](https://doi.org/10.1111/j.1365-2966.2007.11489.x)
- McQuinn, M., Zahn, O., Zaldarriaga, M., Hernquist, L., & Furlanetto, S. R. 2006, *ApJ*, 653, 815, doi: [10.1086/505167](https://doi.org/10.1086/505167)
- Mellema, G., Koopmans, L. V. E., Abdalla, F. A., et al. 2013, *Experimental Astronomy*, 36, 235, doi: [10.1007/s10686-013-9334-5](https://doi.org/10.1007/s10686-013-9334-5)
- Mertens, F. G., Mevius, M., Koopmans, L. V. E., et al. 2020, *MNRAS*, 493, 1662, doi: [10.1093/mnras/staa327](https://doi.org/10.1093/mnras/staa327)
- Mesinger, A. 2010, *MNRAS*, 407, 1328, doi: [10.1111/j.1365-2966.2010.16995.x](https://doi.org/10.1111/j.1365-2966.2010.16995.x)
- Mesinger, A., & Furlanetto, S. 2007, *ApJ*, 669, 663, doi: [10.1086/521806](https://doi.org/10.1086/521806)
- Mesinger, A., Furlanetto, S., & Cen, R. 2011, *MNRAS*, 411, 955, doi: [10.1111/j.1365-2966.2010.17731.x](https://doi.org/10.1111/j.1365-2966.2010.17731.x)
- Mondal, R., Bharadwaj, S., & Datta, K. K. 2018, *MNRAS*, 474, 1390, doi: [10.1093/mnras/stx2888](https://doi.org/10.1093/mnras/stx2888)
- Mondal, R., Shaw, A. K., Iliev, I. T., et al. 2020, *MNRAS*, 494, 4043, doi: [10.1093/mnras/staa1026](https://doi.org/10.1093/mnras/staa1026)
- Moore, D. F., Aguirre, J. E., Parsons, A. R., Jacobs, D. C., & Pober, J. C. 2013, *ApJ*, 769, 154, doi: [10.1088/0004-637X/769/2/154](https://doi.org/10.1088/0004-637X/769/2/154)
- Morales, M. F., Hazelton, B., Sullivan, I., & Beardsley, A. 2012, *ApJ*, 752, 137, doi: [10.1088/0004-637X/752/2/137](https://doi.org/10.1088/0004-637X/752/2/137)
- Morales, M. F., & Hewitt, J. 2004, *ApJ*, 615, 7, doi: [10.1086/424437](https://doi.org/10.1086/424437)
- Murray, S., Greig, B., Mesinger, A., et al. 2020, *The Journal of Open Source Software*, 5, 2582, doi: [10.21105/joss.02582](https://doi.org/10.21105/joss.02582)
- Ocvirk, P., Gillet, N., Shapiro, P. R., et al. 2016, *MNRAS*, 463, 1462, doi: [10.1093/mnras/stw2036](https://doi.org/10.1093/mnras/stw2036)
- O'Shea, B. W., Wise, J. H., Xu, H., & Norman, M. L. 2015, *ApJL*, 807, L12, doi: [10.1088/2041-8205/807/1/L12](https://doi.org/10.1088/2041-8205/807/1/L12)
- Paciga, G., Albert, J. G., Bandura, K., et al. 2013, *MNRAS*, 433, 639, doi: [10.1093/mnras/stt753](https://doi.org/10.1093/mnras/stt753)
- Parsons, A. R., Backer, D. C., Foster, G. S., et al. 2010, *AJ*, 139, 1468, doi: [10.1088/0004-6256/139/4/1468](https://doi.org/10.1088/0004-6256/139/4/1468)
- Planck Collaboration, Aghanim, N., Akrami, Y., et al. 2020, *A&A*, 641, A6, doi: [10.1051/0004-6361/201833910](https://doi.org/10.1051/0004-6361/201833910)
- Poher, J. C., Ali, Z. S., Parsons, A. R., et al. 2015, *ApJ*, 809, 62, doi: [10.1088/0004-637X/809/1/62](https://doi.org/10.1088/0004-637X/809/1/62)
- Pratley, L., & Johnston-Hollitt, M. 2020, *ApJ*, 894, 38, doi: [10.3847/1538-4357/ab6e64](https://doi.org/10.3847/1538-4357/ab6e64)
- Pritchard, J. R., & Loeb, A. 2012, *Reports on Progress in Physics*, 75, 086901, doi: [10.1088/0034-4885/75/8/086901](https://doi.org/10.1088/0034-4885/75/8/086901)
- Riseley, C. J., Galvin, T. J., Sobey, C., et al. 2020, *PASA*, 37, e029, doi: [10.1017/pasa.2020.20](https://doi.org/10.1017/pasa.2020.20)
- Robertson, B. E., Ellis, R. S., Furlanetto, S. R., & Dunlop, J. S. 2015, *ApJL*, 802, L19, doi: [10.1088/2041-8205/802/2/L19](https://doi.org/10.1088/2041-8205/802/2/L19)
- Rohlfs, K., & Wilson, T. L. 2004, *Tools of radio astronomy*

- Rosdahl, J., Blaizot, J., Aubert, D., Stranex, T., & Teyssier, R. 2013, *MNRAS*, 436, 2188, doi: [10.1093/mnras/stt1722](https://doi.org/10.1093/mnras/stt1722)
- Santos, M. G., Ferramacho, L., Silva, M. B., Amblard, A., & Cooray, A. 2010, *MNRAS*, 406, 2421, doi: [10.1111/j.1365-2966.2010.16898.x](https://doi.org/10.1111/j.1365-2966.2010.16898.x)
- Sault, R. J., Hamaker, J. P., & Bregman, J. D. 1996, *A&AS*, 117, 149
- Scott, D., & Rees, M. J. 1990, *MNRAS*, 247, 510
- Shaw, J. R., Sigurdson, K., Pen, U.-L., Stebbins, A., & Sitwell, M. 2014, *ApJ*, 781, 57, doi: [10.1088/0004-637X/781/2/57](https://doi.org/10.1088/0004-637X/781/2/57)
- Shaw, J. R., Sigurdson, K., Sitwell, M., Stebbins, A., & Pen, U.-L. 2015, *PhRvD*, 91, 083514, doi: [10.1103/PhysRevD.91.083514](https://doi.org/10.1103/PhysRevD.91.083514)
- Shimwell, T. W., Tasse, C., Hardcastle, M. J., et al. 2019, *A&A*, 622, A1, doi: [10.1051/0004-6361/201833559](https://doi.org/10.1051/0004-6361/201833559)
- Smirnov, O. M. 2011, *A&A*, 527, A107, doi: [10.1051/0004-6361/201116434](https://doi.org/10.1051/0004-6361/201116434)
- Tingay, S. J., Goeke, R., Bowman, J. D., et al. 2013, *PASA*, 30, e007, doi: [10.1017/pasa.2012.007](https://doi.org/10.1017/pasa.2012.007)
- Trac, H., & Cen, R. 2007, *ApJ*, 671, 1, doi: [10.1086/522566](https://doi.org/10.1086/522566)
- Trott, C. M., Jordan, C. H., Midgley, S., et al. 2020, *MNRAS*, 493, 4711, doi: [10.1093/mnras/staa414](https://doi.org/10.1093/mnras/staa414)
- Van Eck, C. L., Haverkorn, M., Alves, M. I. R., et al. 2019, *A&A*, 623, A71, doi: [10.1051/0004-6361/201834777](https://doi.org/10.1051/0004-6361/201834777)
- van Haarlem, M. P., Wise, M. W., Gunst, A. W., et al. 2013, *A&A*, 556, A2, doi: [10.1051/0004-6361/201220873](https://doi.org/10.1051/0004-6361/201220873)
- Wytthe, J. S. B., & Loeb, A. 2004, *Nature*, 427, 815, doi: [10.1038/nature02336](https://doi.org/10.1038/nature02336)
- Zahn, O., Lidz, A., McQuinn, M., et al. 2007, *ApJ*, 654, 12, doi: [10.1086/509597](https://doi.org/10.1086/509597)
- Zahn, O., Mesinger, A., McQuinn, M., et al. 2011, *MNRAS*, 414, 727, doi: [10.1111/j.1365-2966.2011.18439.x](https://doi.org/10.1111/j.1365-2966.2011.18439.x)
- Zaldarriaga, M., Furlanetto, S. R., & Hernquist, L. 2004, *ApJ*, 608, 622, doi: [10.1086/386327](https://doi.org/10.1086/386327)
- Zaldarriaga, M., & Seljak, U. 1997, *PhRvD*, 55, 1830, doi: [10.1103/PhysRevD.55.1830](https://doi.org/10.1103/PhysRevD.55.1830)